Structure and Physiological Function of the Human KCNQ1 Channel Voltage Sensor Intermediate State

Keenan C. Taylor,[1,2,†] Po Wei Kang,[3,†] Panpan Hou,[3,†] Nien-Du Yang,[3] Georg Kuenze,[2,4] Jarrod A. Smith,[1,2] Jingyi Shi,[3] Hui Huang,[1,2] Kelli McFarland White,[3] Dungeng Peng,[1,2,5] Alfred L. George Jr.[6], Jens Meiler[2,4,7], Robert L. McFeeters[8], Jianmin Cui[3]*, and Charles R. Sanders[1,2,9]*

[1]*Department of Biochemistry, Vanderbilt University, Nashville, TN 37240, USA*

[2]*Center for Structural Biology, Vanderbilt University, Nashville, TN 37240, USA*

[3]*Department of Biomedical Engineering, Center for the Investigation of Membrane Excitability Disorders, and Cardiac Bioelectricity, and Arrhythmia Center, Washington University, St. Louis, MO 63130, USA*

[4]*Departments of Chemistry and Pharmacology, Vanderbilt University, Nashville, TN 37240, USA*

[5]*Department of Medicine, Division of Clinical Pharmacology, Vanderbilt University Medical Center, Nashville, TN, 37232, USA*

[6]*Department of Pharmacology, Northwestern University Feinberg School of Medicine, Chicago, IL, 60611, USA*

[7]*Department of Bioinformatics, Vanderbilt University Medical Center, Nashville, TN 37232, USA*

[8]*Department of Chemistry, University of Alabama in Huntsville, Huntsville, AL 35899, USA*

[9]*Department of Medicine, Vanderbilt University Medical Center, Nashville, TN 37232, USA*

***Corresponding authors:**

Charles R. Sanders, chuck.sanders@vanderbilt.edu

Jianmin Cui, jcui@wustl.edu

[†]These authors contributed equally to this work: Keenan C. Taylor, Po Wei Kang, Panpan Hou

Short Title: KCNQ1 Voltage Sensor Intermediate State

Impact Statement: The intermediate state conformation of the human KCNQ1 potassium channel voltage sensor domain was determined, validated, and shown to be conductive under physiological conditions.

Abstract

Voltage-gated ion channels feature voltage sensor domains (VSDs) that exist in three distinct conformations during activation: resting, intermediate, and activated. Experimental determination of the structure of a potassium channel VSD in the intermediate state has previously proven elusive. Here, we report and validate the experimental three-dimensional structure of the human KCNQ1 voltage-gated potassium channel VSD in the intermediate state. We also used mutagenesis and electrophysiology in *Xenopus laevis* oocytes to functionally map the determinants of S4 helix motion during voltage-dependent transition from the intermediate to the activated state. Finally, the physiological relevance of the intermediate state KCNQ1 conductance is demonstrated using voltage-clamp fluorometry. This work illuminates the structure of the VSD intermediate state and demonstrates that intermediate state conductivity contributes to the unusual versatility of KCNQ1, which can function either as the slow delayed rectifier current (I_{Ks}) of the cardiac action potential or as a constitutively active epithelial leak current.

Introduction

Voltage-gated potassium (K_V) channels are critical for electrical signaling in excitable cells where they drive action potential termination. In K_V channels, the voltage sensor domains (VSDs) undergo specific conformational changes during membrane depolarization to activate channel opening. Previous studies revealed that K_V VSDs activate sequentially from the initial resting state to an experimentally resolvable intermediate state and then to the activated state[1-19]. The movement associated with VSD activation then induces the channel pore domain to open and conduct ionic current. Accordingly, the structural basis underlying VSD conformational change during activation constitutes a fundamental aspect of K_V channel voltage-dependent gating. Despite the importance of VSDs in voltage-dependent gating, an experimental structure for the intermediate state of a K_V VSD has not been reported. Here we present and functionally validate the three-dimensional structure of the human voltage-gated potassium channel KCNQ1 (K_V7.1) VSD in the intermediate state.

Although numerous high-resolution structures of voltage-gated ion channels VSD are available[15,20-27], all experimental VSD structures were determined at 0 mV membrane potential due to the inability to control the membrane potential in the model membrane media use for structural studies. Because 0 mV represents a physiologically depolarized potential for voltage-gated ion channels, nearly all structures of VSDs are thought to represent the depolarized or "up" conformation. This technical challenge has historically complicated structure determination for VSDs in intermediate and resting state conformations. Nevertheless, prior studies have applied varied strategies to characterize VSD structures of voltage-gated channels in alternate conformations. These studies have employed a variety of approaches, including exploiting metal affinity cross-linking to resolve the HCN channel VSD in the hyperpolarized conformation[28],

78 applying site-directed mutagenesis and cysteine crosslinking to bias a Na_V VSD into the resting
79 conformation[27], utilizing a VSD-binding toxin to trap a Na_V VSD in the deactivated state[26], and
80 employing Ca^{2+} to bias a TPC1 channel Ca^{2+}-sensitive VSD into resting and activated
81 states[24,29]. Despite extensive structural studies, an experimental structure for the intermediate
82 state of the KCNQ1 channel VSD has proven elusive. The lack of high-resolution KCNQ1 VSD
83 structures in kinetically significant conformations along the activation pathway represents a
84 major gap in our knowledge of the structural basis of KCNQ1 VSD activation.
85
86 A second challenge in structure-function studies of K_V VSDs, such as the KCNQ1 VSD, in non-
87 activated conformations involves functional validation. The most common functional technique
88 to validate K_V channel structures involves measuring ionic currents by voltage or patch clamp
89 experiments. In most K_V channels, it is thought that the pore domain opens to conduct current
90 only upon VSD transition into the fully activated state. This implies that traditional ionic current
91 measurements are blind to VSD occupation of the resting state or the intermediate state, as
92 both VSD states are thought not to induce pore conduction. Following this line of logic, even if
93 high-resolution VSD structures in the intermediate state were to be determined, the lack of
94 straightforward functional electrophysiology tests to discriminate between VSD conformations of
95 non-conducting channel states (e.g. resting state vs. intermediate state) presents a challenge
96 for functional validation. In this regard, it is significant that the VSD of the KCNQ1 K_V channel is
97 thought to populate an intermediate state that promotes a conductive state of the pore
98 domain[11,12,19], providing a pathway to functional validation of a VSD structure proposed to
99 represent the intermediate state.
100
101 KCNQ1 is a K_V channel that plays multiple physiological roles. When paired with the KCNE1
102 accessory protein, KCNQ1 provides the delayed-rectifier I_{Ks} current of the cardiac action

potential[30-35]. Loss of function or aberrant gain of function caused by heritable mutations in KCNQ1 causes several different arrhythmias, which include long QT syndrome (LQTS)[36-38]. Alternatively, when paired with accessory protein KCNE3, KCNQ1 plays an important role as a leak channel to help maintain ion homeostasis in epithelial cells[30,39,40]. KCNQ1 adopts the canonical structural organization of the K_V superfamily in which the central homotetrameric pore domain is flanked by four VSDs, each with four transmembrane helical segments (S1-S4). Each KCNQ1 VSD exhibits sequential activation[3,9-12], similar to other K_V channels such as the *Drosophila* Shaker channel[2,5-7]. However, while both Shaker and KCNQ1 conduct current when their VSDs adopt the activated conformation, KCNQ1 is distinctive in that it can also conduct current when its VSDs occupy the intermediate conformation[11-13,19].

The intermediate conductance of KCNQ1 channels offers an opportunity to overcome the challenge to conventional electrophysiology of discriminating between KCNQ1 VSD in the resting state vs. the intermediate state. Moreover, we have previously shown that the KCNQ1 intermediate and activated conductances feature distinct auxiliary subunit regulation and pharmacology[11,12,19]. KCNQ1 thus presents an ideal platform for VSD structure-function studies, as traditional electrophysiology techniques can readily distinguish between the resting, intermediate, and activated VSD states. In this study, we determine the structure of the human KCNQ1 VSD and then take advantage of the distinct KCNQ1 intermediate and activated conductances to provide functional evidence that supports this VSD structure as representing the intermediate state rather than the activated or resting states. The cryo-EM structure of the *Xenopus* KCNQ1 determined in dodecylmaltoside (DDM) micelles by the MacKinnon lab appears to represent a channel with a closed pore and flanking VSD domains that populate the fully activated state[22]. The MacKinnon lab also determined the structure of human KCNQ1 in complex with KCNE3[41]. The structures of the *Xenopus* and human KCNQ1 VSDs determined by

the MacKinnon lab are similar. Whether the VSD in the cryo-EM structures represents the fully activated state is also experimentally addressed in this paper. Lastly, we provide evidence to demonstrate that the conductive intermediate state of the KCNQ1 channel is physiologically relevant and contributes to the channel's functional versatility.

Results

NMR structure of the KCNQ1 voltage sensor domain

It has long been known that voltage sensor domains fold autonomously, as reflected by the fact that voltage-gated proton channels are single domain monomeric VSDs[42-44] and also by studies showing that VSDs excised from K_V channels or other voltage-regulated proteins fold independently and yield experimental 3-D structures that are consistent with their conformations in the context of intact channels[23,45]. Indeed, solution nuclear magnetic resonance (NMR) methods have previously been used to determine the activated state structure of the VSD of the KvAP channel from a hyperthermophilic microorganism[46,47]. The NMR-determined structure of the human voltage-gated proton channel H_V1 was also recently reported[48].

Structural studies of the isolated human KCNQ1 VSD spanning from the S0 segment preceding the S1-S4 transmembrane domain through the middle of the S4-S5 link were undertaken using solution NMR spectroscopy of the protein under conditions where it is solubilized in detergent micelles composed of a lipid-like detergent. Screening of suitable model membrane conditions for solution NMR of the isolated human KCNQ1 VSD was previously described and led to the conclusion that, among the various model membrane conditions tested, micelles formed by lyso-myristoylphosphatidylglycerol (LMPG) or lyso-palmitoylphosphatidylglycerol (LPPG) yielded

NMR spectra of superior quality[49]. A similar result was recently reported for preliminary NMR studies of the isolated *Shaker* channel VSD[50]. The lysophospholipids are among the most phospholipid-like detergents available and are known to be generally mild and non-denaturing[51,52]. We conducted the studies of this work in LMPG rather than LPPG micelles (see NMR spectra in Figure 1) because a recent study indicated that the wild type KCNQ1 VSD adopts a stable fold in this medium[53]. This was further supported in the present work by the fact that paramagnetic relaxation enhancements (PREs) of spin-labeled VSD samples revealed a transmembrane topology consistent with the voltage sensor fold (Figure 1-figure supplement 1). We therefore proceeded with structural studies of the human KCNQ1 VSD in LMPG micelle conditions.

The backbone amide ^{1}H, ^{13}C, and ^{15}N resonances and also the side chain methyl peaks of KCNQ1 were assigned using 3D NMR methods (see Figure 1 and Methods). We then collected a series of distinct classes of NMR restraints as summarized in Table 1: backbone torsion angles based on chemical shifts (Figure 1-figure supplement 2), short and long-range ^{1}H-^{1}H NOE-derived distances (Figure 1-figure supplement 3), long-range distances from PREs, and backbone ^{1}H-^{15}N residual dipolar couplings (RDCs). PREs involve use of single site spin-labeling to introduce spectroscopic beacons into the VSD that lead to distance-dependent peak broadening. Care was taken to verify that single cysteine mutations and subsequent spin-labeling did not disrupt the protein structure. Indeed, for several sites mutation and/or spin labeling was found to be disruptive of structure, in which cases PRE data was not acquired. While PRE-determined NMR structures have been shown to be robustly reliable[54-57], long-range NOEs were also incorporated into structure calculations to improve the precision and accuracy of the ensemble. The chemical shift, PRE, and NOE-determined ensemble was refined against measured 1H-15N backbone RDCs, confirming the structure with an independent data set. Care

also was taken to ensure that no subset of the NOE data had an unduly influential impact on the final ensemble of structures (see Methods).

The ensemble of KCNQ1 VSD structures determined by the NMR data and the Xplor-NIH progam[58] is illustrated in Figure 2-figure supplement 1A, with structural statistics in Table 1. Because structural studies of membrane proteins in micelles sometimes are complicated by micelle-based distortion of native structure[6,59,60] we took extra steps to account for and correct any such distortions. Specifically, ten members of the NMR ensemble were selected (based on the root mean squared deviation—r.m.s.d.—to the mean coordinates) for NMR data-restrained molecular dynamics (MD) in a hydrated dimyristoylphosphatidylcholine (DMPC) bilayer. After 100 nsec of restrained MD, the restraints were turned off and the MD trajectories were allowed to continue for another 190-200 nsec to see if the NMR-defined structure would “hold”. Analysis of an ensemble of 10 centroid structures generated from the final 100 nsec of the lowest energy trajectory revealed that this ensemble continued to satisfy the NMR data (Table 1). This final VSD structural ensemble is illustrated in Figure 2A (PDB ID: 6MIE). Figure 2-figure supplement 1 shows that the combined restrained/unrestrained molecular dynamics phase of structural refinement resulted in only modest changes relative to the starting XPLOR-NIH NMR conformational ensemble. We emphasize that PDB 6MIE continues to satisfy the NMR restraints (Table 1). In this final ensemble the NMR data defines the protein fold and some side chain conformations. However, the side chain conformations for the key residues highlighted in Figure 3A were not directly restrained by any of the experimental data, but were determined by the force fields operative in the X-plorNIH simulated annealing protocol and in subsequent MD trajectories.

As will be described later in this paper, functional studies indicate that the VSD structure determined herein (Figures 2-4) represents the *intermediate* state conformation along the VSD activation pathway. The preparation of a sample in which the isolated WT VSD occupies the previously structurally-uncharacterized intermediate state appears to be the fortuitous consequence of performing studies in LMPG micelles, which stabilizes this otherwise difficult-to-access state, enabling it to be subjected to structural characterization.

The NMR-determined human KCNQ1 VSD conformation features a short surface amphipathic N-terminal helix (S0) and four transmembrane helices (S1-S4), followed by part of the S4-S5 linker, the latter of which was disordered (Figure 2A). Comparison of this structure to that of the *Xenopus* KCNQ1 VSD determined by cryo-EM in β-dodecyl-D-maltopyranoside (DDM) micelles (Figures 2B, 3, and 4)[22] reveals important differences.

Positively charged amino acids are located along the transmembrane S4 helix of potassium channel VSDs and some of these charges, commonly known as “gating charges”, confer voltage-sensitivity to channel functions. We will refer to the gating charges as R1 through R6, numbered from the N-terminal end to the C-terminal end of the S4 segment (Figure 3D). During membrane depolarization, the S4 helix moves from its resting state outward toward the extracellular space[61]. During this movement the gating charges successively pair with conserved acidic residues within the VSD[62], including residues of the “charge transfer center”, which additionally contains an aromatic residue acting as a “hydrophobic plug”[63,64]. Critical residues that coordinate gating charge movement include the acidic residue E1 (E160 in human KCNQ1) and the charge transfer center residues E2 (E170), D202 and the aromatic plug residue F0 (F167, Figure 3). Pairwise electrostatic interactions between the positive gating charges in S4 and the negatively charged S2/S3 residues help solvate the positive S4 residues

in the hydrophobic membrane interior to stabilize the VSD. In KCNQ1, electrophysiological and modeling studies suggested that the activated state of the VSD involves pairing of E1 with gating charge site R4 (R237)[3,10,11,65]. This pairing was observed in the cryo-EM structure of the KCNQ1 VSD (Figures 3B and 4B)[22], suggesting that the VSD seen in that structure reflects the activated state. By inference, the activated state is likely stabilized by additional interactions of the charge transfer residues E2 and F0 on S2 and D202 on S3 with residue H5 (H240)[22]. On the other hand, we observed a different arrangement of S4 charge pairings with S2 residues in the NMR structure of the human KCNQ1 VSD. These differences were the consequence of S4 being translated by ~ 5.4 Å along the bilayer normal toward the extracellular side during the transition from the NMR structure to the cryo-EM structure (Figure 3A-C). In the NMR structure R2 (R231) pairs with E1 (Figure 3A and 4A), which is postulated to be a crucial stabilizing interaction for the intermediate VSD state based on previous electrophysiological results[3,10,11]. This strongly suggests that the NMR structure represents the intermediate VSD state. Additional observed interactions that likely contribute to intermediate state stabilization include interaction of R4 with charge transfer residues E2 and D202, as well as interaction of Q3 (Q234, corresponding to R3 in most other voltage-gated channels) with F0 (Figures 3A,D and 4A).

Functional validation of distinct KCNQ1 voltage sensor domain structures

To validate that the NMR structure of the VSD faithfully represents the intermediate state and that the VSD seen in the cryo-EM structure represents the activated state, we tested whether the paired-residue interactions revealed by these two structures can be demonstrated functionally. To this end, we used a double charge reversal mutagenesis strategy (Figure 5A-C). Mutation of gating charges in S4 to a negatively charged residue leads to strong electrostatic repulsion between the S2/S4 helices and consequent VSD loss of function[10] (Figure 5B).

However, a simultaneous positively charged mutation in S2 provides a favorable electrostatic interacting partner for the S4 mutation and re-stabilizes the VSD (Figure 5C). Importantly, the electrostatic interactions between the S2/S4 helices are only energetically favorable when the mutated charge in S4 is aligned with the paired mutation in S2 (Figure 5C). The double mutations thus arrest the VSD conformation as dictated by the S4/S2 charge reversal mutation sites, yielding constitutively opened channels[10,11,62,65] (Figure 5).

We next looked for functional readouts to determine whether the arrested VSD conformations correspond to the intermediate or activated VSD states. We took advantage of the fact that KCNQ1 conducts current with distinct properties when its VSDs adopt either intermediate or activated states[11]. The canonical open state associated with the activated VSD is referred to as the “activated-open” (AO) state, while the distinct open state associated with the intermediate VSD is referred to as the “intermediate-open” (IO) state. The AO and the IO states, and by inference the activated and intermediate VSD states, can be discriminated by two functional metrics. First, KCNQ1 co-expression with the accessory subunit KCNE1 selectively suppresses IO-state current by preventing pore opening when the VSD adopts the intermediate state[11]. In addition, KCNE1 co-expression amplifies AO-state currents, in part by increasing single channel conductance[11,12], and possibly also by affecting VSD-pore coupling. Figure 5D summarizes KCNE1 regulation of the KCNQ1 IO-state and AO-state currents. These KCNE1 regulatory effects slow current activation (due to IO state suppression) and enhance current amplitude (due to AO state potentiation) of the WT KCNQ1 channels (Figure 5E)[11]. Second, the IO state is selectively inhibited by the KCNQ channel modulator XE991 compared to the AO state[11]. Thus, current recordings in response to KCNE1 co-expression (Figure 5) and to XE991 exposure (Figure 6) allow us to test whether the S2-S4 interactions seen in the two structures correspond to the intermediate or activated VSD states.

We generated two classes of mutants designed to promote specific interactions based on the interacting residue pairs involving S2 and S4 observed in the differing NMR and cryo-EM VSD structures (Figures 4, 5A). The first class of mutants was derived from the NMR-structure: E170R paired with R237E (E2R/R4E), and F167R with both Q234E and D202N (F0R/Q3E/D202N). The second class of mutants was based on interacting residue pairs observed in the cryo-EM structure (Figures 4, 5A): F167R paired with H240E and D202N (F0R/H5E/D202N). An additional charge transfer center mutation D202N (in S3) was included along with the S4/S2 double charge reversal mutations F0R/Q3E and F0R/H5E. We had expected the double mutants F0R/Q3E and F0R/H5E to arrest S2-S4 registration, thereby yielding constitutively opened channels. However, both double mutants retain some levels of voltage-dependence in activation (Figure 5-figure supplement 5), suggesting that the double mutant only modestly stabilized the VSDs in their respective states. This voltage-dependence was eliminated upon the addition of the D202N mutation (Figure 5F-H), suggesting that D202 interfered with the ability of F0R/Q3E and F0R/H5E to arrest S2-S4 registration. This result also indicates that D202 is important for interacting with S4 gating charges during activation. As shown in Figure 5F-H, our designed KCNQ1 mutants (E2R/R4E, F0R/Q3E/D202N, and F0R/H5E/D202N) yielded constitutively open channel with minimal voltage dependence, consistent with the idea that the mutations strongly stabilize the VSDs in the intermediate or activated states by arresting the S2-S4 registration. Because the mutants were designed based on the NMR and cryo-EM VSD structures, these results also indicate that the VSDs in these mutant channels were arrested in the conformations corresponding the respective VSD structures. Next, we probed whether the VSD of these mutant channels corresponded to the functional intermediate and activated states by examining whether these KCNQ1 mutant channels were in the IO or AO state (Figures 5, 6). We note that our experiments stabilized all

four VSDs of KCNQ1 in the same conformation, thus we do not consider the pore conformation in the case of asymmetrical VSD states.

We first tested if these mutant channels exhibited the respective KCNE1 regulatory effect for the IO or AO state (Figure 5D). To test whether KCNE1 suppresses or enhances ionic currents of our mutants, we controlled for channel expression levels by injecting the mutant channel RNA in *Xenopus* oocytes with and without KCNE1 RNA co-injection on the same day. We then made recording using the same mutant with and without KCNE1 RNA co-injection on the same day post injection (see Methods). Because channel expression was not controlled across mutant channels (e.g. E2R/R4E vs. F0R/Q3E/D202N), we did not interpret current amplitudes between different mutants. The mutants E2R/R4E and F0R/Q3E/D202N resulted in constitutive opening of the channel (Figure 5 F,G), which is consistent with stabilization of the intermediate VSD state by interactions between E2-R4 and F0-Q3. Consistently, KCNE1 co-expression strongly suppressed currents conducted by both mutants as shown by the current exemplar and average I-V curves (Figure 5F,G), confirming that interactions of these mutant residues stabilize the IO state (Figure 5D). The mutant F0R/H5E/D202N also resulted in constitutively open channels similar to E2R/R4E and F0R/Q3E/D202N (Figure 5H). However, in contrast to the prior two mutants, KCNE1 co-expression greatly enhanced F0R/H5E/D202N current as illustrated by the exemplar currents (note scale bars) and average I-V curves (Figure 5H), confirming the hypothesis that F0-H5 interaction stabilizes the AO state (Figure 5D).

We also found that KCNE1 co-expression could distinguish between the double mutants F0R/Q3E and F0R/H5E that retain some levels of voltage dependence. First, KCNE1 co-expression suppressed current amplitudes of the F0R/Q3E mutant (Figure 5-figure supplement 5C) but greatly enhanced current amplitudes of the F0R/H5E mutant (Figure 5-figure

supplement 5E). Second, KCNE1 co-expression right-shifted the conductance-voltage (G-V) relation of F0R/Q3E mutant significantly more than that of F0R/H5E (Figure 5-figure supplement 5C,E), indicating that F0R/Q3E favors the IO state and F0R/H5E promotes the AO state. These results are consistent with those of the triple mutants F0R/Q3E/D202N and F0R/H5E/D202N (Figure 5G,H). Altogether, the KCNE1 co-expression experiments unambiguously indicate that the KCNQ1 mutants designed according to the NMR and cryo-EM VSD structures occupy the IO and the AO states, respectively (Figure 5F-H, Figure 5-figure supplement 1). These KCNE1 co-expression results thus indicate that the NMR structure of the KCNQ1 VSD corresponds to the intermediate state, while the cryo-EM structure of the KCNQ1 VSD populates the activated state.

We next examined whether XE991 pharmacology might consistently identify these mutant channels at the IO or AO state. Previous studies found that the KCNQ modulator XE991 at 5 μM preferentially inhibits the IO-state current over the AO-state current, as summarized in Figure 6A[11]. We started by probing the effect of XE991 on the KCNQ1 E2R/R4E mutant. We first recorded oocytes expressing the KCNQ1 E2R/R4E channels in control ND96 solution. The channels were held at -20 mV and pulsed to +40 mV for 4 seconds (test pulse) and -40 mV for 2 seconds (tail pulse) every 20 seconds. Figure 6B visualizes exemplar E2R/R4E mutant current amplitudes at the end of the 40-mV test pulse over time throughout the experiment. After the E2R/R4E current amplitude reached a stable level under control conditions (Figure 6B, black arrow and current trace), we applied 5 μM XE991 and continued recording until the current amplitude reached steady state (Figure. 6B, red arrow and current trace). The E2R/R4E current amplitude was relatively small at around 1 to 1.5 μA (Figures 5F, 6B). The smaller current amplitude may lead to poor estimation of E2R/R4E current inhibition by XE991 due to endogenous oocyte current contamination. We therefore subsequently applied 150 μM

chromanol 293B, a selective I_{Ks} and KCNQ1 blocker, to the bath containing 5 μM XE991 (Figure 6B). We calculated XE911 inhibition of E2R/R4E currents by first subtracting the current after chromanol application (Figure 6B, blue arrow and current trace) from the currents under control and 5 μM XE991 conditions (Figure 6B, black and red currents respectively). As plotted in Figure 6C, the resulting chromanol-subtracted currents represent XE991 inhibition of E2R/R4E currents without endogenous current contamination. The percent XE991 inhibition was calculated using the ratio of the chromanol-subtracted current amplitudes of the control and XE991 conditions (see Methods). As illustrated by the exemplar and the average inhibition bar plot (Figures 6C, black to red currents, and 6D), XE991 robustly inhibited ~80% of E2R/R4E currents, suggesting that the E2R/R4E mutant stabilizes the IO state (Figure 6A).

Likewise, we found that 5 μM XE991 also significantly inhibited F0R/Q3E/D202N mutant currents as demonstrated in Figure 6E-F, with an average inhibition of ~75% (Figure 6G). This result confirms that the F0R/Q3E/D202N mutant stabilizes the IO state, similar to the E2R/R4E mutant. In contrast, 5 μM XE991 was far less effective at inhibiting F0R/H5E/D202N currents, as shown in the exemplar and average bar plots, with an average inhibition ~20% (Figure 6H-J). This result indicates that the F0R/H5E/D202N mutant promotes the AO state and thus conducts current resistant to XE991 inhibition (Figure 6A). Moreover, the XE991 pharmacology experiments revealed consistent findings with the double mutants F0R/Q3E and F0R/H5E, in which the F0R/Q3E mutant was robustly inhibited by 5 μM XE991 inhibition while the F0R/H5E was insensitive to 5 μM XE991 (Figure 5-figure supplement 5F-J). These double mutant results agree with data from the triple mutants F0R/Q3E/D202N and F0R/H5E/D202N (Figure 6E-J), further supporting the notion that F0-Q3 and F0-H5 interactions are found in IO and the AO states respectively.

Critically, data from these XE991 experiments corroborate the IO- and AO-state discrimination between VSD mutants deduced from the KCNE1 co-expression data (Figure 5). Taken together, these two sets of results (Figures 5, 6, Figure 5-figure supplement 1) strongly suggest that E2-R4 and F0-Q3 are interactions found in the KCNQ1 VSD intermediate state, while the F0-H5 interaction is present in the activated state. These data validate that the NMR VSD structure represents a conformation that corresponds to the stable intermediate state of the VSD during voltage-dependent activation, while the VSD in the cryo-EM structure represents the activated state.

KCNQ1 VSD activation motion from the intermediate to the activated state

Comparison of the two VSD structures (Figure 3C) reveals a pronounced S4 helix movement relative to the rest of the VSD upon transition from the intermediate to the activated state, with a ~5.4 Å translation of S4 toward the extracellular direction accompanied by unraveling of the N-terminal end of this helix, perhaps as a result of its transition into a well-hydrated extracellular environment (Figure 3C). Consequently, the S4 helix of the intermediate state is longer by two additional turns between V221 and G229, suggesting a simultaneous loss of the secondary structure in the N-terminal portion of S4 during the transition from the intermediate to activated state. Other helices, especially the extracellular half of S3, undergo only modest translations, as evident in an overlay of the two structures (Figure 3C). In both structures, the S4 charges form ion pairs with E1, E2, and D202, but with different registrations. Our functional studies demonstrated that these ion pairs provide much of the energy to stabilize the VSD in the intermediate and activated states during voltage-dependent activation (Figures 5 and 6), thereby delimiting the trajectory of VSD motions during the intermediate-to-activated state transition.

Physiological role of the intermediate state of the KCNQ1 voltage sensor

Our study so far presents a structure of the KCNQ1 VSD and provides functional evidence that the structure represents a stable intermediate conformation along the KCNQ1 VSD activation pathway. In our functional validation, we extensively utilized the distinct KCNQ1 intermediate conductive IO state induced by the intermediate VSD state. However, little is known regarding the physiological role of this conductive IO state. Both this report and prior studies indicate that the auxiliary subunit KCNE1 suppresses the IO state[11] (Fig. 5). In cardiac myocytes, KCNQ1 is known to complex with KCNE1 to generate the I_{Ks} current required for cardiac action potential termination[31,32,66,67]. The KCNQ1 IO state thus likely minimally impact normal cardiac physiology. What role might the KCNQ1 intermediate VSD state and its associated conductive IO state play in normal physiology? To answer this question, we look beyond cardiac tissues.

KCNQ1 is unusual in that its functional properties vary profoundly in association with different tissue-specific KCNE accessory proteins[35,68]. In epithelial cells, KCNQ1 associates with KCNE3 to form a “leak” potassium current essential for epithelial ion homeostasis[30,39,40,69,70]. KCNE3 renders KCNQ1 current constitutively active in physiological voltage ranges as shown in Figure 7A, by contrast to the time- and voltage-dependent cardiac I_{Ks} (KCNQ1/KCNE1). These strikingly distinct KCNQ1 currents fit their respective tissue-specific needs. On one hand, cardiac physiology demands the I_{Ks} channel to conduct late during an action potential. This explains why KCNE1 suppresses the IO state and restricts KCNQ1 pore opening to VSD transition into the activated conformation[11]. On the other hand, epithelial physiology requires KCNQ1+KCNE3 to conduct over wide-ranging voltages, including more hyperpolarized potentials where the intermediate VSD state is energetically favored over the activated VSD

state. We therefore hypothesized that KCNE3 may render KCNQ1 constitutively active in part by utilizing the intermediate VSD conformation and the IO state.

To examine whether the KCNQ1/KCNE3 complex conducts significant current with the IO state, we undertook voltage-clamp fluorometry (VCF) experiments. VCF tracks KCNQ1 VSD transitions by a labeled fluorophore attached to the S3-S4 linker, which changes fluorescence emission during voltage-dependent activation[9,11,13,71-73]. The KCNQ1 fluorescence-voltage (F-V) relation exhibits two components that can be well-fit by a double Boltzmann function (F_1 and F_2 in Figure 7A,B), which correspond to VSD sequential transitions from resting to intermediate (F_1) and from intermediate to activated (F_2) states[11,12]. Selective regulation of distinct VSD transitions can be inferred from changes to F_1 and F_2. Comparison of the G-V relation with the F-V relation provides insight into IO vs. AO state regulation. For example, it has been shown that KCNE1 co-expression specifically causes a hyperpolarized shift in the F_1 component of the F-V relation but depolarizes the G-V curve to follow the F_2-V relation (Figure 7A)[9,11,12]. Our previous study indicated that this phenomenon derives from a mechanism in which KCNE1 eliminates the IO state by preventing pore opening when the VSD is in the intermediate state, such that I_{Ks} represents conductance only in the AO state[11,12]. KCNE3 co-expression has also been demonstrated to induce a hyperpolarizing shift in the F-V relation, suggesting that KCNE3 promotes channel opening by shifting the voltage dependence of VSD activation[71,72].

A careful inspection of VCF measurements reveals that KCNE3, like KCNE1, also specifically hyperpolarizes the F_1 component while having little effect on the F_2 component (Figure 7A,B, see also[71,72]). However, unlike KCNE1, KCNE3 shifted the G-V curve in a hyperpolarizing direction to follow the F_1-V curve (Figure 7A). This led us to hypothesize that unlike KCNE1, KCNE3 association does not prevent pore opening when the VSD adopts the intermediate

state. This was tested by co-expressing KCNE3 with KCNQ1-F351A, a mutant known to be non-conductive when the VSD occupies the intermediate state[11,12]. The KCNQ1-F351A/KCNE3 channel complex maintained a hyperpolarized F_1 component, but the G-V relationship changed to track the F_2-V curve, confirming that the currents observed for wild type KCNQ1/KCNE3 at negative voltages are conducted by the IO state (Figure 7B). KCNE3 also preserves the AO state as shown by two observations. First, residual pore opening observed in KCNQ1-F351A/KCNE3 indicates that the AO state is intact, as the KCNQ1-F351A channels cannot conduct in the IO state (Figure 7B). Second, subtraction of the instantaneous current from KCNQ1-WT/KCNE3 current reveals a time- and voltage-dependent current which tracks the F_2 component (Figure 7C, GV_2 curve), suggesting that the time-dependent fraction of KCNQ1-WT/KCNE3 channels conduct at the AO state at high voltages. Taken together, these results demonstrate that KCNQ1/KCNE3 conducts with both the IO and the AO states. However, our VCF data indicate that the intermediate VSD state is more favorably occupy at hyperpolarized voltages (Figure 7A), suggesting that the IO state may significantly contribute to physiological KCNQ1/KCNE3 currents.

To further examine whether KCNQ1/KCNE3 preferentially conducts at the IO state, we compared XE991 inhibition of KCNQ1/KCNE3 and KCNQ1/KCNE1. Figure 7D shows the overlays of KCNQ1, KCNQ1/KCNE1, and KCNQ1/KCNE3 current traces stabilized in control ND96 solutions (black) and solutions containing 5 μM XE991 (grey, blue, red). Although the KCNQ1 AO-state current is resistant to 5 μM XE991, KCNE1 was previously shown to sensitize the AO state to permit some XE991 inhibition[11]. Still, KCNE1 and KCNE3 induced distinct XE991 blocking kinetics of KCNQ1 currents during each pulse of channel activation. Figure 7E illustrates the time-dependent inhibition of XE991 by plotting the current amplitudes under 5 μM XE991 conditions divided by that of the control, with the x-axis indicating time after the voltage

was stepped to +40 mV. KCNQ1/KCNE1 current featured much slower XE991 time-dependent block compared to KCNQ1 alone, suggesting that KCNQ1/KCNE1 primarily conducts at the AO state. By contrast, the KCNQ1/KCNE3 current exhibited rapid XE991 inhibition with kinetics faster than KCNQ1 alone. This result suggests that KCNQ1/KCNE3 preferentially conducts IO-state current, which is sensitive to XE991. Taken together, our results demonstrate that in the physiological voltage range (-80 to +50 mV) the KCNQ1/KCNE3 complex preferentially populates the conductive IO state over the AO state, as promoted by the occupancy of the VSDs in the intermediate state (Figure 7A).

Discussion

This study took advantage of the unique ability of LMPG micelles to stabilize the intermediate state of the human KCNQ1 VSD, leading to determination of its structure using a robust approach combining NMR spectroscopy with data-restrained MD. The intermediate state VSD structure complements both the previous activated state *Xenopus* KCNQ1 VSD structure in DDM micelles determined using cryo-EM[22] and homology models for human KCNQ1 in both the fully activated and resting states[74]. Both the new NMR structure and the cryo-EM VSD structures are consistent with structure-function results from previous studies of KCNQ1 and were also rigorously validated in this work by additional electrophysiological studies. Determination and validation of the KCNQ1 VSD structures in the intermediate and activated states furnishes critical information for understanding the voltage-dependent activation of KCNQ1 and interactions with KCNE accessory subunits. The intermediate and activated VSD structures are seen to be distinctly different, which is as expected because they are coupled to channel conductance in ways that exhibit very different sensitivities to KCNE1 and drug binding. We acknowledge that the intermediate state VSD structure was determined in isolation from the

rest of the channel and that future studies will be required to elucidate exactly how it is coupled to the pore to promote the IO conductance state.

Even with the limitation indicated immediately above, the intermediate state VSD structure can be used in conjunction with the cryo-EM structure of KCNQ1[22] and with available models for both resting and fully activated human KCNQ1[74] to illuminate KCNQ1 pharmacology, physiology, and how some of the dozens of known LQTS disease mutations located in the VSD result to channel loss of function or dysfunction[34,53,75]. Moreover, the KCNQ1 VSD intermediate state structure can be used as a template to model the intermediate state voltage sensors of other voltage-gated channels, such as the Shaker potassium channel[2,4-7], and voltage-gated Na channels[76], which are believed to activate in a step-wise manner with S4 gating charges sequentially pairing with the charge transfer center and other acidic residues.

This work utilizes KCNQ1's unique intermediate conductance to provide functional electrophysiology evidence that the VSD structure presented here truly represents the intermediate state conformation. We presented functional validation based on two independent metrics, auxiliary subunit KCNE1 regulation and XE991 pharmacology (Figures 5 and 6). While the precise mechanism by which KCNE1 suppresses the IO state and enhances the AO state remains unclear, the fact that KCNE1 co-expression unambiguously discriminates channel mutants designed to stabilize the NMR VSD structure vs. the cryo-EM VSD structure constitutes compelling evidence that the two structures represent distinct functional KCNQ1 VSD states. Moreover, pharmacological studies of the same mutants by XE991 fully corroborate KCNE1 co-expression results, indicating that our functional validation data are robust and not dependent on any single functional result. By contrast, use of functional measurements to illuminate the properties of the intermediate state versus those of the activated state would be very

challenging for K_V channels that do populate an intermediate VSD state, but for which the pore is thought to only conduct current when its VSDs occupy the activated state, such as the Shaker channel. In the case of the Shaker channel, functional electrophysiology would be unable to distinguish the intermediate state vs. the resting state of the VSD, as both states yield no ionic currents. KCNQ1 thus represents a particularly suitable platform for structure-function study of the intermediate state in K_V VSDs.

In addition to utilizing KCNQ1's intermediate conductance as a functional probe, this work also suggests a possible physiological role for the KCNQ1 intermediate conductance. We demonstrated that under physiological conditions where KCNQ1 is paired with KCNE3 as an accessory subunit, the channel is maximally conductive over a wide range of transmembrane voltages. Depending on the transmembrane electrical potential, conductance may be a mix of the IO and AO states, as we observe that KCNE3 preserves both open states (Figure 7). Two cryo-EM structures of the full-length KCNQ1/KCNE3/calmodulin complex with and without PIP_2 were published during the revision of this manuscript[41]. In both new structures, the VSDs adopt the fully activated conformation at 0 mV membrane potential[41], consistent with our finding that KCNQ1/KCNE3 complex conducts some AO-state current at depolarized voltages. Nevertheless, our VCF and XE991 results demonstrate that that KCNE3 may more favorably stabilize the KCNQ1 VSDs in the intermediate state at more hyperpolarized voltages (-150 to -40 mV, Figure 7A, F_1 curve for KCNQ1/KCNE3). The primary function of the KCNQ1/KCNE3 complex is to serve as a leak channel in epithelial cells[30,39,40,69,70]. As epithelial cells are non-excitable cells and not physiologically subject to the highly depolarizing membrane potentials required to activate substantial AO state conductance, the IO state conductance likely constitutes the bulk of the physiological KCNQ1/KCNE3 leak K^+ current in epithelial cells. Thus, the IO state is not merely a transient state on the pathway from resting to the AO state. Rather,

551 the data suggests that IO is itself an essential conductive state under some physiological
552 conditions. KCNE1 and KCNE3 therefore promote different open states to confer exceptional
553 functional versatility, uniquely tailoring KCNQ1 so that it can satisfy distinct physiological needs
554 in different cell types and tissues.
555
556 **Material and Methods**
557

Key Resources Table				
Reagent type (species) or resource	**Designation**	**Source or reference**	**Identifiers**	**Additional information**
gene (human)	KCNQ1	HUGO Gene Nomenclature Committee (HGNC)	Gene ID: 3784; HGNC:6294	
gene (human)	KCNE1	HUGO Gene Nomenclature Committee (HGNC)	Gene ID: 3753; HGNC:6240	
gene (human)	KCNE3	HUGO Gene Nomenclature Committee (HGNC)	Gene ID: 10008; HGNC:6243	
strain, strain background (*Escherichia coli*)	CT19 transaminase deficient strain	Dr. David Waugh, US National Cancer Institute PMID: 8914274		Used for special isotopic labelling of the KCNQ1 VSD for use in NMR studies.
strain, strain background (*Escherichia coli*)	Rosetta/ C43(DE3)	Sigma-Aldrich	Catalog number 70954	Used for uniform isotopic labelling of KCNQ1 and amino acid-specific labelling for NMR.

recombinant DNA reagent	pET16b expression plasmid encoding tagged human KCNQ1-(100-249)	PMID: 24606221		Used to express the human KCNQ1 VSD for NMR structural studies
biological sample (include species here)	*Xenopus* oocytes (*Xenopus* laevis, female)	This paper	RRID:XEP_Xla	*Xenopus* laevis purchased from Nasco, Fort Atkinson, WI
recombinant DNA reagent	pcDNA3.1 encoding human KCNQ1 or KCNE1	This paper	RRID:Addgene_111452	For site-directed mutagenesis
commercial assay or kit	mMessage T7 polymerase kit	Applied Biosystems-Thermo Fisher Scientific	AM1344	
chemical compound, drug	XE991	Millipore Sigma	CAS #: 122955-42-4	
chemical compound, drug	Chromanol 293B	Millipore Sigma	CAS #: 163163-23-3	
chemical compound, drug	Alexa Fluor 488 C5 maleimide	Molecular Probes, Eugene, OR	Catalog #: A10254	
software	Topspin 3.2	Bruker (Scientific Instruments Company)	RRID: SCR_014227	NMR data collection and processing.
software	MDD and qMDD interface	URL: mddnmr.spektrino.com/ PMID: 21161328		NMR data processing

software	NMRFAM-SPARKY	PMID: 25505092 URL: https://nmrfam.wisc.edu/nmrfam-sparky-distribution/		NMR data analysis and resonance assignments.
software	TALOS-N	PMID: 25502373 URL: spin.niddk.nih.gov/bax/software/TALOS-N/		Determination of secondary structure from NMR chemical shift data.
software	CHARMM-GUI	PMID: 25130509 URL: www.charmm-gui.org/		Preparation of starting structures of the KCNQ1 VSD in lipid bilayers for MD restrained MD simulations.
software	XPLOR-NIH	PMID: 28766807 URL: https://nmr.cit.nih.gov/xplor-nih/		Structure calculations using NMR data restraints
software	GPU-accelerated AMBER 16	URL: https://amberrmd.org/ PMID: 16200636		Program for execution of MD simulations.
software	Lipid 17 AMBER	PMID: 24803855 URL: https://amberrmd.org/AmberModels.php		Force field used for MD simulations.

software	CPPTRAJ	PMID: 26583988 URL: https://amber-md.github.io/		Analysis of MD trajectories following simulations.
software	PatchMaster	HEKA	RRID:SCR_000034	Electrophysiology data collection
software	IGOR	Wavemetrics, Lake Oswego, OR	RRID:SCR_000325	Electrophysiology data analysis
software	Clampfit	Axon Instruments, Sunnyvale, CA	RRID:SCR_011323	Electrophysiology data analysis
software	Sigmaplot	SPSS, San Jose, CA	RRID:SCR_003210	Electrophysiology data analysis and visualization
Software	MATLAB	MathWorks, MA	RRID:SCR_001622	Electrophysiology data analysis
sequence-based reagent	For site-directed mutagenesis	This paper	PCR primers	PCR primers seq for mutations made in this study (each mutation utilized 2 primers: b and c). E170R-b:cacgtacCTGgtcccgaagaacaccac; E170R-c: cgggacCAGgtacgtggtccgcctc; R237E-b: gcatcTCcaggatctgcaggaag; R237E-c:cagatcctgGAgatgctacacgtcgac F167R-b: ccgtcccgCGgaacaccaccagcac; F167R-c: gtgttcCGcgggacggagtacg Q234E-b:ggatctCcaggaagcggatgccc; Q234E-

				c: catccgcttcctgGagatcctg aggatgcta H240E- b: cggtcgacCTCtagcatcct caggatc H240E-c: gctaGAGgtcgaccgccaggg D202N-b: cgatgaggtTAatgatggaaat gggcttc D202N-c: ccatcatTAacctcatcgtggtcg tg F351A-b: ggcaGCGcccgagccaagaa tcc F351A-c: gctcgggCGCtgccctgaaggt gcag C214A-b: cttggaTcccacCGCgaggac cacca C214A-c: cGCGgtgggAtccaaggggc aggtg G219C-b: cctgaCacttggaTcccacCG C G219C-c: ggAtccaagtGtcaggtgtttgc cacg C331A-b: gacagagaaTGCggaggcg atggtcttc C331A-c: ctccGCAttctctgtctttgccatc

Constructs, mutagenesis, and expression

Point mutations of the KCNQ1 channel were engineered using overlap extension and high-fidelity PCR. Each mutation was verified by DNA sequencing. The cRNA of mutants was synthesized using the mMessage T7 polymerase kit (Applied Biosystems-Thermo Fisher Scientific).

The human KCNQ1 (GenBank accession number AF000571) VSD was cloned into a pET16b expression vector as previously described[49]. The pET16b expression construct included an N-terminal His tag of the sequence MGHHHHHHG followed by KCNQ1 residues 100 – 249. Single

amino acid mutations were generated by QuikChange site-directed mutagenesis and verified by sequencing to confirm the presence of the desired codon substitutions. For expression, the *E. coli* strain C43(DE3) harboring the pRARE plasmid (encoding rare codon tRNAs) was transformed with the KCNQ1-VSD pET16b vector. Transformants were cultured overnight in 3 mL of LB media containing 100μg/mL ampicillin and 30 μg/mL chloramphenicol at 37°C. The following morning, each liter of M9 media was inoculated with 1 mL of starter culture. M9 minimal media supplemented with appropriate antibiotics, MEM vitamins (Mediatech), and 50 μM $ZnCl_2$. As required, 1g of $^{15}HN_4Cl$ and 2g ^{13}C-glucose (U-^{13}C6, 99%) was included per liter of M9 to produce U-^{13}C,^{15}N-labeled samples. Cultures were incubated at 22°C with rotatory shaking and expression was induced upon reaching an OD_{600} of 0.8 by the addition of 1 mM IPTG. After 24 hours the cells were harvested, and the pellet was stored at -80°C. To produce uniformly-^{2}H,^{13}C,^{15}N-labeled samples, cells were first conditioned for growth in 100% D_2O medium in the following manner. First, cells were cultured in 3 mL of D_2O LB for 3 to 5 hours at 37°C until flocculent and then used to inoculate 30 mL 100% D_2O M9 media. After 12 to 16 hours of incubation, once the cells reached mid-log growth phase, 15 mL of the culture was used to inoculate 1L of 100% D_2O M9. Large-scale growth continued at 37°C until the OD_{600} reach 0.5, at which point the temperature was adjusted to 22°C. The protocol then proceeded as described for the preparation of double-labeled samples. Appropriate antibiotics were included at all steps.

Amino acid-selective isotopic labeling was performed as previously described[49]. The transaminase deficient strain of *E. coli*, CT19 (a gift from Dr. David Waugh of the US National Cance Institute), was used to reduce ^{15}N-labeled amino acid scrambling. CT19 cells were transformed with pET16b-Q1-VSD plasmid and grown in 4L of LB media containing with 10 mg/L ampicillin, 100 mg/L Kanamycin, and 20 mg/L tetracycline at 37°C. Once the culture

reached an OD_{600} of 0.6 the cells were harvested at 2,500 g for 15 min. The pellet was gently resuspended in 1L of M9 media containing 0.2 g of the ^{15}N-labeled amino acid of interest. Additionally, the media was supplemented with 0.5 g of alanine, phenylalanine, leucine, isoleucine, aspartate, tyrosine, and 0.1 g tryptophan (excluding the amino acid to be labeled in each case). The growth then proceeded as described previously. Four samples were prepared, each with a single ^{15}N-labeled amino acid, including Val, Leu, Ile, or Phe. Additionally, reverse isotopic labeling of Arg residues was carried out by the addition of excess ^{14}N-Arg (1 g/L) in $^{15}NH_4Cl$ M9 media prior to induction.

Protein purification

Cell pellets were resuspended at a ratio of 1 g per 20 mL lysis buffer (75 mM Tris-HCl, 300 mM NaCl, and 0.2 mM EDTA (ethylenediaminetetraacetic acid, pH 7.8) with 5 mM $Mg(Ac)_2$, 0.2 mg/ml PMSF (phenylmethylsulfonyl fluoride), 0.02 mg/ml DNase, 0.02 mg/ml RNase and 0.2 mg/ml lysozyme and tumbled for 30 minutes. The cells were lysed by probe sonication for 10 minutes and a cycle time of 10 seconds on ice at 4°C. Inclusion bodies were then isolated by centrifugation at 20,000 g for 20 minutes at 4°C. The pellet was resuspended by homogenization and the sonication step was repeated once more. After cell lysis, the pellet was resuspended at a ratio of 1 g pre-lysis pellet weight per 10 mL buffer A (40 mM HEPES, 300 mM NaCl, pH 7.5) containing 0.5% (w/v) dodecylphosphocholine (DPC) (Anatrace, Maumee, OH) and 2 mM TCEP and tumbled overnight at 4°C to solubilize the inclusion bodies. The following morning, insoluble debris was removed by centrifugation at 20,000 g for 20 minutes. The supernatant was then incubated with 0.2 mL Superflow Ni(II)-NTA (Qiagen, Germantown, MD) per 1 g pre-lysis pellet weight for at least 1 hour at 4°C. After batch binding, the Ni(II)-NTA was then packed into a gravity-flow column and washed with 10 column volumes (CV) of buffer A containing 0.5% (w/v) DPC and 2 mM TCEP. Impurities were eluted by washing with 12 CV of

buffer A containing 0.5% DPC, 2 mM TCEP, and 60 mM imidazole (pH 7.5). Detergent exchange was performed by washing the column with 10 CV of buffer A containing 0.2 % (w/v) LMPG (lyso-myristoylphosphatidylglycerol) and 2 mM TCEP. The KCNQ1-VSD was eluted in buffer A containing 0.2% (w/v) LMPG, 2 mM TCEP, and 500 mM imidazole until A_{280} as monitored continuously returned to the baseline level (3 - 4 CV). Typical Q1-VSD yields were 2 – 3 mg per liter of growth. The eluent was concentration ten-fold by centrifugation (3,700 g, 4°C) in an Amicon Ultra cartridge (10,000 molecular weight cut-off). The sample was then diluted ten-fold in NMR buffer (40 mM MES, 0.5 mM EDTA, 2 mM TCEP, pH 5.5). This process was repeated a total of four times. The KCNQ1-VSD concentration was determined by A_{280} using an extinction coefficient of 34950 M^{-1} cm^{-1}. Samples were flash frozen in liquid nitrogen and stored at -80°C.

Preparation of spin-labeled samples

A cysteine-free KCNQ1-VSD construct was generated with the following amino acid substitutions: C122S, C136A, C180S, and C214A. Combinations of amino acid substitutions were tested to identify the combination that produced only very minimal perturbation of the TROSY-HSQC spectrum relative to the native KCNQ1-VSD. Notability, KCNQ1 cysteine substitutions have been shown to not significantly perturb channel function[77]. Eight single-cysteine constructs were used for MTSL labeling and PRE measurements: K121C, T144C, T155C, T177C, C180, C214, T224C, and M238C. Each single-cysteine construct was U-^{15}N labeled and purified as previously described[49]. To the rougly 8 ml of Ni(II)-NTA elution, DTT and EDTA were added to final concentrations of 2.5 mM and 1 mM respectively. The pH was then carefully adjusted from 7.5 to 6.5 by multiple additions of 0.2 mL 1 M HCl. Prior to a 2 hour 25°C incubation with gentle tumbling, the volume was reduced to 0.5 mL by centrifugal ultrafiltration (Amicon Ultra cartridge 10,000 MWCO, 3,700 g, 4°C). Incubation continued overnight after the

addition of MTSL (1-oxyl-2,2,5,5-tetramethylpyrroline-3-methyl-methanethiosulfonate, Santa Cruz Biotechnology) to 10 mM from a 0.25 M stock in DMSO. Argon gas was used to displace any air within the incubation tube. The following morning, samples were diluted to 10 mL of buffer A (40 mM HEPES, 300 mM NaCl, pH 7.5) and then concentrated 20-fold. After repeating this step, MTSL-labeled protein was batch bound to 1 mL Ni(II)-NTA and incubated for 1-hour. After batch binding, the Ni(II)-NTA was then packed into a gravity-flow column and washed with 16 column volumes (CV) of buffer A containing 0.2% (w/v) LMPG. The sample was eluted and prepared for NMR experiments as previously described[49].

Preparation of aligned Q1-VSD for residual dipolar coupling measurements

A neutral 5% polyacrylamide gel (50:1 acrylamide:bis-acrylamide molar ratio) was polymerized in a cylindrical casing with a 6 mm inner diameter. After two hours, the gel plug was displaced and equilibrated with NMR buffer in three steps. In the first step, the gel was incubated in 50 mL of buffer (40 mM MES, 0.5 mM EDTA, pH 5.5) for six hours. This step was repeated once, and then in the final step the gel was equilibrated against NMR buffer (40 mM MES, 2 mM TCEP, 0.05% LMPG (w/v), 0.5 mM EDTA, 5% D_2O, pH 5.5). Subsequently, the gel was then cut to 12 mm in length and transferred to a 1.5 mL cryotube and incubated with ca. 0.6 mL of 0.4 mM ^{15}N-KCNQ1-VSD for two days. The gel was then stretched into an open-ended 5 mm NMR tube (4.2 mm inner diameter, New Era). The remaining KCNQ1-VSD solution was transferred to a 3 mm NMR tube and used to measure J_{NH} couplings under isotropic conditions.

NMR data collection and processing

All NMR data were collected at 50 °C on Bruker Avance spectrometers at 600 MHz (14.4 T), 800 MHz (18.7 T), or 900 MHz (21.1 T) each equipped with a cryoprobe. NMR data were processed in Topspin 3.2 or qMDD[78] and analyzed with NMRFAM-Sparky[79]. NMR samples were

composed of 0.2 – 0.4 mM KCNQ1-VSD, 50 mM MES, 0.5 mM ETDA, 2 mM TCEP, and 50 to 80 mM LMPG. Between 2.5% and 7.5% (v/v) D_2O was added to each sample prior to data acquisition. A shaped tube containing 0.4 mL of 0.4 mM KCNQ1-VSD was used for all triple resonance experiments. Proton chemical shifts were referenced to internal DSS while ^{15}N and ^{13}C chemical shifts were referenced indirectly to DSS using absolute frequency ratios. Non-uniform sampling (NUS) was used to increase resolution per unit time of acquisition for triple resonance backbone and side-chain experiments[80].

Chemical shift assignments

Backbone $^{1}H^{N}$, ^{15}N, $^{13}C^{a}$,$^{13}C^{b}$, and $^{13}C'$ chemical shifts were assigned using TROSY versions of three-dimensional (3D) HNCA, HNCO, HN(CO)CA, and HNCACB experiments at 900 MHz on a ^{2}H,^{13}C,^{15}N-KCNQ1-VSD sample[81]. Triple resonance backbone experiments were carried out using NUS with 25% sparse sampling. In addition, an ^{15}N-edited 3D NOESY-TROSY was recoded with an NOE mixing time (τ_{mix}) of 150 ms at 900 MHz. Two-dimensional (2D) TROSY HSQC spectra were recorded on samples with selectively labeled amino acids to aid in resonance assignments. Backbone amide peaks for 140 out of 147 non-proline residues (95%) were assigned.

Side-chain assignments were based on data from NOESY and amide correlated TOCSY experiments. 3D TROSY-(H)C(CO)NH-TOCSY and TROSY-H(CCO)NH-TOCSY experiments were carried out using NUS with 50% sparse sampling recorded on a ^{13}C,^{15}N-labeled sample at 600 MHz. Additionally, an H(C)CH-COSY was recorded using NUS with 42% sparse sampling. 2D ^{13}C-edited HSCQ and 3D ^{13}C-edited NOESY (τ_{mix} = 150 ms) experiments were recorded on a uniformly ^{13}C,^{15}N-labeled sample in 99% D_2O (v/v) at 900 MHz. A 3D ^{15}N-edited NOESY (τ_{mix}

= 120 ms) at 900 MHz was collected using an ^{15}N-labeled sample. Additionally, methyl optimized 2D ^{13}C-edited HSCQ and 3D ^{13}C-edited NOESY (τ_{mix} = 200 ms) experiments were recorded on a ^{13}C,^{15}N-labeled sample in deuterated LMPG (FBReagents) and 99% D_2O (v/v) at 900 MHz. Methyl groups for 58 out of 68 (85%) residues were assigned (Ala 10/10, Thr 6/8, Ile 9/11, Val 18/22, Leu 15/17).

Paramagnetic relaxation enhancements (PREs)

PRE measurements were carried out as described previously[82]. Briefly, two TROSY HSQC spectra were acquired with matched parameters and processed identically on each spin-labeled sample at 900 MHz. The first spectrum was collected under paramagnetic conditions and then reduced by the addition of pH-matched ascorbic acid to 20 mM. Importantly, the change in sample volume after addition of ascorbic acid was under 1%. The second spectrum was then collected under diamagnetic conditions. The intensity ratios and the diamagnetic sample linewidths were used to determine distances between the backbone amide proton and site of the spin label[56].

Residual dipolar couplings (RDCs)

Backbone ^{1}H-^{15}N RDC data was acquired by measuring an HSQC and TROSY spectrum for the aligned and isotropic KCNQ1-VSD samples. The ^{1}H couplings were obtained from doubling the resonance frequency difference between the HSQC and TROSY peaks in the ^{15}N dimension. In the isotropic and aligned samples this frequency difference corresponds to J_{NH} and $J_{NH}+D_{NH}$ respectively. The initial estimates of the axial (Da) and rhombic (R) components of the alignment tensor were derived from the largest observed D_{NH}-value and the program calcTensor (distributed with XPLOR-NIH) using the KCNQ1-VSD ensemble determined in the absence of RDC restraints[58].

720

721 **Structure calculations**

722 Structure calculations were performed using XPLOR-NIH via simulated annealing protocols in
723 three steps[58], as summarized in this paragraph. In the first step, starting with an extended
724 polypeptide the secondary structure was defined using local NOE-derived distance and
725 backbone torsion restraints. Hydrogen bond distance and geometry restraints were then
726 incorporated based on two criteria (i) observed helices in the initial ensemble, and (ii) chemical
727 shift index analysis[83]. In the second step, long-range NOE- and PRE- derived restraints were
728 added to define the tertiary contacts of the VSD. First local NOEs were implemented,
729 contributing to identification of well-defined secondary structural elements. Then high
730 confidence long-range NOEs were incorporated, resulting in a loosely defined ensemble.
731 Additional long-range NOEs were added through an iterative process until a precise ensemble
732 was achieved. As described at the end of this section of the Methods, care was taken to verify
733 the structural outcome was not unduly overdependent on any subset of long-range NOE data. In
734 the third and final step, the top 10% of the structural ensemble were refined with RDC data.
735 Details for all three steps are as follows.

736

737 Backbone torsion angle restraints were determined using ^{15}N, $^{13}C'$,$^{13}C^{\alpha}$, and $^{13}C^{\beta}$, chemical
738 shifts using the program TALOS-N[84]. Only dihedral angle restraints classified as “strong” with a
739 confidence score of 7 or higher were used with an error set to 20°. Resonances in
740 transmembrane helices S1, S2, and S3, exhibited significantly reduced peak amplitudes in 2D
741 spectra as compared to the remainder of the protein. Based on this observation, NOE cross-
742 peaks were divided into two groups and calibrated separately. NOESY spectra cross-peaks
743 were manually assigned (see “Chemical Shifts Assignment” section) and classified based on
744 intensity distribution into one of four groups: strong, medium, weak, and very weak. These

classifications correspond to distance restraints of 1.8 – 2.8, 1.8 – 3.5, 1.8 – 4.5, and 1.8 – 5.5 angstroms. PRE restraints were implemented as the distance between the CB of the spin-labeled residue to the backbone amide hydrogen. Each restraint was categorized into one of three bins based on the intensity ratio between the paramagnetic and diamagnetic (I_{para}/I_{dia}) spectra. For an I_{para}/I_{dia} ratio of less than 0.2 the distance was restrained to between 2 and 18 Å. When the I_{para}/I_{dia} ratio was between 0.2 and 0.8 an explicit distance was calculated and given an uncertainty of $\pm$ 6 Å[56]. Lastly, an I_{para}/I_{dia} ratio great than 0.8 was restrained to between 19 to 100 Å. Only isolated NMR resonances were selected to be incorporated as distance restraints in structure calculations. PREs were observed for S0 in experiments when the spin label was located on either the intra- or extra-cellular face of the VSD, suggesting the S0 helix undergoes motions making the inclusion of PRE-derived distance restraints to this structural element inappropriate. For this reason, no PRE restraints were used for residues within S0.

Structure calculations were conducted in a similar manner to previous work, using standard XPLOR-NIH protocols, where calculations are carried out in four stages: high temperature molecular dynamics, simulated annealing, torsion angle, and Cartesian minimization[82]. In the first stage, the temperature was set to 3,500 K for 20 ps with the following force constants: $k_{bond\ angle}$=0.4 kcal mol^{-1} deg^{-1}; $k_{improper}$=0.4 kcal mol^{-1} deg^{-2}; $k_{backbone\ dihedrals}$=5 kcal mol^{-1} rad^{-1}; k_{NOE}= 20 kcal mol^{-1} Å^{-1}; k_{PRE}= 2 kcal mol^{-1} Å^{-1}. Prior to simulated annealing, force constants were increased over 2 ps: $k_{atom\ radii}$= 0.4-fold to 0.8 fold; $k_{van\ der\ waals}$=0.004 – 4 kcal mol^{-1} Å^{-2}; $k_{bond\ angle}$=0.4 – 1.0 kcal mol^{-1} deg^{-1}; $k_{improper}$= 0.4 – 1.0 kcal mol^{-1} deg^{-2}. During simulated annealing, the temperature was reduced to 100 K in 25 K steps while force constants were increased, k_{NOE}= 20 – 30 kcal mol^{-1} Å^{-1}, k_{PRE}= 2 – 3 kcal mol^{-1} Å^{-1}, and $k_{backbone\ dihederals}$ was set to 200 kcal mol^{-1} rad^{-1}. Distance restraints were enforced by a flat well harmonic and H-bond potentials were included. A total of 150 structures were calculated and the top 15 lowest energy structures

were refined with RDC data. In refinement, the bath temperature was set to 3000 K for 10 ps and then cooled to 25 K in 12.5 steps. RDC restraints were set to 0.05 kcal mol^{-1} Hz^{-2} for the high temperature phase and then ramped to 0.8 kcal mol^{-1} Hz^{-2} during simulated annealing. A total of 150 structures were calculated. The RDC refined ensemble is shown in Figure 2-figure supplement 1A and its structure statistics are presented in Table 1.

XPLOR-NIH calculations were followed by data-restrained molecular dynamics (rMD) refinement in an explicit lipid bilayer using the AMBER16 force field. This step allows the micellar structure to be adjusted in a simulated bilayer to adjust for any micellar distortions, while still enforcing the NMR data restraints. For this, ten structures were selected from the RDC-refined Xplor-NIH ensemble based on r.m.s.d. to the mean coordinates and consistency of S0 orientation with previous experimental results[22]. These ten structures then were solvated in an explicit DMPC bilayer using the CHARMM-GUI server[85]. Notably, a DMPG bilayer was also tested as a rMD environment and no significant differences in restraint violations as compared to DMPC were observed. Simulations used the Lipid17 AMBER lipid force field and the ff14SB force field[86]. Using GPU-accelerated AMBER16 [87], restrained minimization of each structure was performed stepwise. Over 30,000 steps first the lipids and then the aqueous solvent was minimized with the protein atoms restrained to initial positions. Then over 20,000 steps the protein and subsequently the entire system was minimized with NMR restraints. The force constants for distance and angle restraints were set to 10 kCal/mol/$Å^2$ and 20 kCal/mol/rad^2 respectively. The system was then heated to 323K in six steps. In the first step, the system was heated to 50K and the protein backbone, sidechains, lipid head groups, lipid tails, and ions were each restrained with force constants of 10, 5, 2.5, 2.5 and 10 kCal/mol/$Å^2$ respectively. In the subsequent five steps, the system was heated from 50 K to 323 K iteratively. In each repetition the force constants were reduced until the final round where only the protein backbone was

795 restrained with a force constant of 0.1 kCal/mol/Å^2. The system was then equilibrated for 5 ns
796 with protein atoms constrained to starting position. After equilibration, all atoms were released,
797 and NMR restraints were ramped to 100% weight over 20 ps. Each trajectory ran with NMR
798 restraints for a total 100 ns using constant pressure periodic boundary conditions and
799 anisotropic pressure scaling. Each trajectory was then extended at least another 190 ns without
800 NMR restraints, with the results then being tested to verify they remained consistent with the
801 NMR restraints. The unrestrained trajectory seeded with the lowest energy rMD structure shifted
802 only 3 Å for all residues and 2 Å for transmembrane helices (Figure 2,-figure supplement 1D,E),
803 leading to the final ensemble, (PDB ID: 6MIE). The final ensemble is composed of the centroid
804 of the most populated cluster for each 10 ns block of time over the last 100 ns of the trajectory
805 and is shown in Figure 2-figure supplement 1B. Clustering was preformed using the dbscan
806 algorithm in CPPTRAJ[87]. Each member of this final ensemble was then scored with the NMR
807 restraints and found to be consistent with experimental data (Table 1). A comparision of the
808 XplorNIH and MD-refined ensemble is shown in Figure 2-figure supplement 1.
809
810 To verify that the ensemble was not dependent on small subset of the NOE restraints, structure
811 calculations were repeated where a random fraction of long-range NOE restraints were
812 excluded (10%). This was repeated a total of 10 times, where in each run a different fraction of
813 data was withheld, such that all long-range NOE-derived restraints were excluded at least once.
814 In all of these calculations, the same overall fold and ion pairings of gating residues were
815 observed as in the final reported structure. The primary difference between the 10 runs was the
816 precision to which the ensemble was determined, which demonstrates that the final structures
817 (represented by PDB 6MIE, see also Figure 2) are not dependent on any specific subset of
818 long-range NOE-derived restraints.
819

Oocyte expression

Stage V or VI oocytes were obtained from *Xenopus laevis* by laparotomy. All procedures were performed in accordance with the protocol approved by the Washington University Animal Studies Committee (Protocol # 20190030). Oocytes were digested by collagenase (0.5 mg/ml, Sigma Aldrich, St Louis, MO) and injected with channel cRNAs (Drummond Nanoject, Broomall). Each oocyte was injected with cRNAs (9.2 ng) of WT or mutant KCNQ1, with or without KCNE cRNAs (2.3 ng). Injected cells were incubated in ND96 solution (in mM): 96 NaCl, 2 KCl, 1.8 $CaCl_2$, 1 $MgCl_2$, 5 HEPES, 2.5 CH_3COCO_2Na, 1:100 Pen-Strep, pH 7.6) at 18°C for at least 2 days before recording.

Two-electrode voltage clamp (TEVC) and voltage-clamp fluorometry (VCF)

Microelectrodes (Sutter Instrument, Item #: B150-117-10) were made with a puller (Sutter Instrument, P-97), and the resistances were 0.5-3 MΩ when filled with 3 M KCl solution. Ionic currents were recorded by TEVC in ND96 bath solutions. Whole-oocyte currents were recorded using a CA-1B amplifier (Dagan, Minneapolis, MN) with Patchmaster (HEKA) software. The currents were sampled at 1 kHz and low-pass-filtered at 2 kHz. All recordings were carried out at room temperature (21–23 °C). For experiments involving comparing the current amplitude of the KCNQ1 channel with and without KCNE1 co-expression, steps were taken to control oocyte channel expression that can confound current amplitude comparison. RNAs encoding for each mutant KCNQ1 channel was injected the same day, with and without KCNE1 RNAs co-injection. The cells injected with the same mutant KCNQ1 RNA were later recorded during the same day after channel expression. This controls for channel expression for each mutant with and without KCNE1 co-expression and allows for current amplitude comparison within each mutant. For XE991 and chromanol 293B experiments, the cells were held at -20 mV holding potential and pulsed to +40 mV (4 seconds) and -40 mV (2 seconds) every 20 seconds. Each cell was first

recorded under control ND96 solution until steady state. Stock XE991 (10 mM) and Chromanol 293B (100 mM) were added after ionic current in control and XE991 solutions reached steady state, respectively. Stock drugs were added to achieve final dilution of 5 μM XE991 and 150 μM chromanol 293B. All cRNA amounts were doubled for VCF experiments to achieve higher surface expression level. Oocytes were incubated for 30 min on ice in 10 μM Alexa 488 C5-maleimide (Molecular Probes, Eugene, OR) in high K^+ solution in mM (98 KCl, 1.8 $CaCl_2$, 5 HEPES, pH 7.6) for labeling. Cells were washed three times with ND96 solution to remove the labeling solution, and recordings were performed in ND96 solution on the CA-1B amplifier setup. Excitation and emission lights were filtered by a FITC filter cube (Leica, Germany, for Alexa 488) and the fluorescence signals were collected by a Pin20A photodiode (OSI Optoelectronics). The signals were then amplified by an EPC10 (HEKA, analog filtered at 200 Hz, sampled at 1 kHz) patch clamp amplifier and controlled by the CA-1B amplifier to ensure fluorescence signals were recorded simultaneously with currents. All other chemicals were from Sigma Aldrich.

Electrophysiology data analysis

Data were analyzed with IGOR (Wavemetrics, Lake Oswego, OR), Clampfit (Axon Instruments, Inc., Sunnyvale, CA), Sigmaplot (SPSS, Inc., San Jose, CA), and custom MATLAB (MathWorks, MA) software. The instantaneous tail currents following test pulses were normalized to the maximal current to calculate the conductance-voltage (G-V) relationship. Because of photo-bleaching, fluorescence signals were baseline subtracted by fitting and extrapolating the first 2 s signals at the -80 mV holding potential. ΔF/F was calculated after baseline subtraction. Fluorescence-voltage (F-V) relationships were derived by normalizing the ΔF/F value at the end of each four-seconds test pulse to the maximal value. F-V and G-V curves were fitted with either one or the sum of two Boltzmann equations in the form $1/(1+\exp(-z^*F^*(V-V_{1/2})/RT))$ where z is

the equivalent valence of the transition, $V_{1/2}$ is the voltage at which the transition is half maximal, R is the gas constant, T is the absolute temperature, F is the Faraday constant, and V is the voltage. Current inhibition from XE991 was calculated by using the steady-state current amplitude at the end of the four-seconds test pulse in control ($I_{control}$) and drug (I_{XE991} or $I_{chromanol}$) solutions. The fraction of XE991 inhibition was calculated by first subtracting $I_{chromanol}$ from $I_{control}$ and I_{XE991} to account for endogenous current contamination. XE991 inhibition fraction was then calculated utilizing the ratio of the chromanol-subtracted current with the following equation:

$$f_{\mathrm{XE991}} = 1 - \frac{I_{\mathrm{XE991}} - I_{\mathrm{chromanol}}}{I_{\mathrm{control}} - I_{\mathrm{chromanol}}} = \frac{I_{\mathrm{control}} - I_{\mathrm{XE991}}}{I_{\mathrm{control}} - I_{\mathrm{chromanol}}} \qquad (1)$$

Acknowledgments: We thank Dr. Ben Mueller for his assistance with the software used in the structural studies, Dr. Kirill Oxenoid for advice on NMR experiments, and Prof. Markus Voehler for technical assistance with NMR experiments. This work was supported by NIH R01 HL122010 (to C.R.S., A.L.G., and J.M.), by R01 NS092570 and R01 HL126774 to J.C., by AHA 18POST34030203 to P.H. and by NIH F32 GM117770 (to K.C.T.).

Competing interests: J.S. and J.C. are cofounders of a startup company VivoCor LLC, which is targeting I_{Ks} for the treatment of cardiac arrhythmia. The authors declare that they have no other competing interests.

Data and materials availability: All data needed to evaluate the conclusions in the paper are present in the paper and/or in the figure supplements and source data files. The NMR chemical shift assignments for the KCNQ1 VSD have been deposited in BioMagResBank (BMRB ID 30517) and the structural ensemble for the KCNQ1 VSD has been deposited into the Protein Databank (PDB ID 6MIE). Correspondence and request for materials should be addressed to J.C. (jcui@wustl.edu) or C.R.S. (chuck.sanders@vanderbilt.edu).

References

1. Sigworth, F. J. (1994) Voltage gating of ion channels, *Q Rev Biophys 27*, 1-40.
2. Bezanilla, F., Perozo, E., and Stefani, E. (1994) Gating of Shaker K+ channels: II. The components of gating currents and a model of channel activation, *Biophys J 66*, 1011-1021.
3. Silva, J. R., Pan, H., Wu, D., Nekouzadeh, A., Decker, K. F., Cui, J., Baker, N. A., Sept, D., and Rudy, Y. (2009) A multiscale model linking ion-channel molecular dynamics and electrostatics to the cardiac action potential, *Proc Natl Acad Sci U S A 106*, 11102-11106.
4. Zagotta, W. N., Hoshi, T., and Aldrich, R. W. (1994) Shaker potassium channel gating. III: Evaluation of kinetic models for activation, *J Gen Physiol 103*, 321-362.
5. Baker, O. S., Larsson, H. P., Mannuzzu, L. M., and Isacoff, E. Y. (1998) Three transmembrane conformations and sequence-dependent displacement of the S4 domain in shaker K+ channel gating, *Neuron 20*, 1283-1294.
6. Jensen, M. O., Jogini, V., Borhani, D. W., Leffler, A. E., Dror, R. O., and Shaw, D. E. (2012) Mechanism of voltage gating in potassium channels, *Science 336*, 229-233.
7. Lacroix, J. J., Pless, S. A., Maragliano, L., Campos, F. V., Galpin, J. D., Ahern, C. A., Roux, B., and Bezanilla, F. (2012) Intermediate state trapping of a voltage sensor, *J Gen Physiol 140*, 635-652.
8. Silverman, W. R., Roux, B., and Papazian, D. M. (2003) Structural basis of two-stage voltage-dependent activation in K+ channels, *Proc Natl Acad Sci U S A 100*, 2935-2940.
9. Barro-Soria, R., Rebolledo, S., Liin, S. I., Perez, M. E., Sampson, K. J., Kass, R. S., and Larsson, H. P. (2014) KCNE1 divides the voltage sensor movement in KCNQ1/KCNE1 channels into two steps, *Nat Commun 5*, 3750.
10. Wu, D., Delaloye, K., Zaydman, M. A., Nekouzadeh, A., Rudy, Y., and Cui, J. (2010) State-dependent electrostatic interactions of S4 arginines with E1 in S2 during Kv7.1 activation, *J Gen Physiol 135*, 595-606.
11. Zaydman, M. A., Kasimova, M. A., McFarland, K., Beller, Z., Hou, P., Kinser, H. E., Liang, H., Zhang, G., Shi, J., Tarek, M., and Cui, J. (2014) Domain-domain interactions determine the gating, permeation, pharmacology, and subunit modulation of the IKs ion channel, *Elife 3*, e03606.
12. Hou, P., Eldstrom, J., Shi, J., Zhong, L., McFarland, K., Gao, Y., Fedida, D., and Cui, J. (2017) Inactivation of KCNQ1 potassium channels reveals dynamic coupling between voltage sensing and pore opening, *Nat Commun 8*, 1730.
13. Osteen, J. D., Barro-Soria, R., Robey, S., Sampson, K. J., Kass, R. S., and Larsson, H. P. (2012) Allosteric gating mechanism underlies the flexible gating of KCNQ1 potassium channels, *Proc Natl Acad Sci U S A 109*, 7103-7108.
14. Swartz, K. J. (2008) Sensing voltage across lipid membranes, *Nature 456*, 891-897.
15. Li, Q., Wanderling, S., Sompornpisut, P., and Perozo, E. (2014) Structural basis of lipid-driven conformational transitions in the KvAP voltage-sensing domain, *Nat Struct Mol Biol 21*, 160-166.

16. Roux, B. (2006) Dissecting the coupling between the voltage sensor and pore domains, *Neuron 52*, 568-569.
17. Sigg, D., Stefani, E., and Bezanilla, F. (1994) Gating current noise produced by elementary transitions in Shaker potassium channels, *Science 264*, 578-582.
18. Vargas, E., Yarov-Yarovoy, V., Khalili-Araghi, F., Catterall, W. A., Klein, M. L., Tarek, M., Lindahl, E., Schulten, K., Perozo, E., Bezanilla, F., and Roux, B. (2012) An emerging consensus on voltage-dependent gating from computational modeling and molecular dynamics simulations, *J Gen Physiol 140*, 587-594.
19. Hou, P., Shi, J., White, K. M., Gao, Y., and Cui, J. (2019) ML277 specifically enhances the fully activated open state of KCNQ1 by modulating VSD-pore coupling, *Elife 8*.
20. Long, S. B., Campbell, E. B., and Mackinnon, R. (2005) Crystal structure of a mammalian voltage-dependent Shaker family K+ channel, *Science 309*, 897-903.
21. Long, S. B., Campbell, E. B., and Mackinnon, R. (2005) Voltage sensor of Kv1.2: structural basis of electromechanical coupling, *Science 309*, 903-908.
22. Sun, J., and MacKinnon, R. (2017) Cryo-EM Structure of a KCNQ1/CaM Complex Reveals Insights into Congenital Long QT Syndrome, *Cell 169*, 1042-1050 e1049.
23. Li, Q., Wanderling, S., Paduch, M., Medovoy, D., Singharoy, A., McGreevy, R., Villalba-Galea, C. A., Hulse, R. E., Roux, B., Schulten, K., Kossiakoff, A., and Perozo, E. (2014) Structural mechanism of voltage-dependent gating in an isolated voltage-sensing domain, *Nat Struct Mol Biol 21*, 244-252.
24. Kintzer, A. F., and Stroud, R. M. (2016) Structure, inhibition and regulation of two-pore channel TPC1 from Arabidopsis thaliana, *Nature 531*, 258-262.
25. Shen, H., Liu, D., Wu, K., Lei, J., and Yan, N. (2019) Structures of human Nav1.7 channel in complex with auxiliary subunits and animal toxins, *Science 363*, 1303-1308.
26. Clairfeuille, T., Cloake, A., Infield, D. T., Llongueras, J. P., Arthur, C. P., Li, Z. R., Jian, Y., Martin-Eauclaire, M. F., Bougis, P. E., Ciferri, C., Ahern, C. A., Bosmans, F., Hackos, D. H., Rohou, A., and Payandeh, J. (2019) Structural basis of alpha-scorpion toxin action on Nav channels, *Science 363*.
27. Wisedchaisri, G., Tonggu, L., McCord, E., Gamal El-Din, T. M., Wang, L., Zheng, N., and Catterall, W. A. (2019) Resting-State Structure and Gating Mechanism of a Voltage-Gated Sodium Channel, *Cell 178*, 993-1003 e1012.
28. Lee, C. H., and MacKinnon, R. (2017) Structures of the Human HCN1 Hyperpolarization-Activated Channel, *Cell 168*, 111-120 e111.
29. Kintzer, A. F., Green, E. M., Dominik, P. K., Bridges, M., Armache, J. P., Deneka, D., Kim, S. S., Hubbell, W., Kossiakoff, A. A., Cheng, Y., and Stroud, R. M. (2018) Structural basis for activation of voltage sensor domains in an ion channel TPC1, *Proc Natl Acad Sci U S A 115*, E9095-E9104.
30. Abbott, G. W. (2016) KCNE1 and KCNE3: The yin and yang of voltage-gated K(+) channel regulation, *Gene 576*, 1-13.
31. Barhanin, J., Lesage, F., Guillemare, E., Fink, M., Lazdunski, M., and Romey, G. (1996) K(V)LQT1 and lsK (minK) proteins associate to form the I(Ks) cardiac potassium current, *Nature 384*, 78-80.
32. Sanguinetti, M. C., Curran, M. E., Zou, A., Shen, J., Spector, P. S., Atkinson, D. L., and Keating, M. T. (1996) Coassembly of K(V)LQT1 and minK (IsK) proteins to form cardiac I(Ks) potassium channel, *Nature 384*, 80-83.

33. Hedley, P. L., Jorgensen, P., Schlamowitz, S., Wangari, R., Moolman-Smook, J., Brink, P. A., Kanters, J. K., Corfield, V. A., and Christiansen, M. (2009) The genetic basis of long QT and short QT syndromes: a mutation update, *Hum Mutat 30*, 1486-1511.
34. Tobelaim, W. S., Dvir, M., Lebel, G., Cui, M., Buki, T., Peretz, A., Marom, M., Haitin, Y., Logothetis, D. E., Hirsch, J. A., and Attali, B. (2017) Ca(2+)-Calmodulin and PIP2 interactions at the proximal C-terminus of Kv7 channels, *Channels (Austin) 11*, 686-695.
35. Liin, S. I., Barro-Soria, R., and Larsson, H. P. (2015) The KCNQ1 channel - remarkable flexibility in gating allows for functional versatility, *J Physiol 593*, 2605-2615.
36. Wu, W., and Sanguinetti, M. C. (2016) Molecular Basis of Cardiac Delayed Rectifier Potassium Channel Function and Pharmacology, *Card Electrophysiol Clin 8*, 275-284.
37. Campuzano, O., Fernandez-Falgueras, A., Lemus, X., Sarquella-Brugada, G., Cesar, S., Coll, M., Mates, J., Arbelo, E., Jorda, P., Perez-Serra, A., Del Olmo, B., Ferrer-Costa, C., Iglesias, A., Fiol, V., Puigmule, M., Lopez, L., Pico, F., Brugada, J., and Brugada, R. (2019) Short QT Syndrome: A Comprehensive Genetic Interpretation and Clinical Translation of Rare Variants, *J Clin Med 8*.
38. Wu, J., Ding, W. G., and Horie, M. (2016) Molecular pathogenesis of long QT syndrome type 1, *J Arrhythm 32*, 381-388.
39. Julio-Kalajzic, F., Villanueva, S., Burgos, J., Ojeda, M., Cid, L. P., Jentsch, T. J., and Sepulveda, F. V. (2018) K2P TASK-2 and KCNQ1-KCNE3 K(+) channels are major players contributing to intestinal anion and fluid secretion, *J Physiol 596*, 393-407.
40. Schroeder, B. C., Waldegger, S., Fehr, S., Bleich, M., Warth, R., Greger, R., and Jentsch, T. J. (2000) A constitutively open potassium channel formed by KCNQ1 and KCNE3, *Nature 403*, 196-199.
41. Sun, J., and MacKinnon, R. (2020) Structural Basis of Human KCNQ1 Modulation and Gating, *Cell 180*, 340-347 e349.
42. DeCoursey, T. E., Morgan, D., Musset, B., and Cherny, V. V. (2016) Insights into the structure and function of HV1 from a meta-analysis of mutation studies, *J Gen Physiol 148*, 97-118.
43. Ramsey, I. S., Moran, M. M., Chong, J. A., and Clapham, D. E. (2006) A voltage-gated proton-selective channel lacking the pore domain, *Nature 440*, 1213-1216.
44. Sasaki, M., Takagi, M., and Okamura, Y. (2006) A voltage sensor-domain protein is a voltage-gated proton channel, *Science 312*, 589-592.
45. Jiang, Y., Lee, A., Chen, J., Ruta, V., Cadene, M., Chait, B. T., and MacKinnon, R. (2003) X-ray structure of a voltage-dependent K+ channel, *Nature 423*, 33-41.
46. Shenkarev, Z. O., Paramonov, A. S., Lyukmanova, E. N., Shingarova, L. N., Yakimov, S. A., Dubinnyi, M. A., Chupin, V. V., Kirpichnikov, M. P., Blommers, M. J., and Arseniev, A. S. (2010) NMR structural and dynamical investigation of the isolated voltage-sensing domain of the potassium channel KvAP: implications for voltage gating, *J Am Chem Soc 132*, 5630-5637.
47. Butterwick, J. A., and MacKinnon, R. (2010) Solution structure and phospholipid interactions of the isolated voltage-sensor domain from KvAP, *J Mol Biol 403*, 591-606.
48. Bayrhuber, M., Maslennikov, I., Kwiatkowski, W., Sobol, A., Wierschem, C., Eichmann, C., Frey, L., and Riek, R. (2019) Nuclear Magnetic Resonance Solution Structure and Functional Behavior of the Human Proton Channel, *Biochemistry 58*, 4017-4027.
49. Peng, D., Kim, J. H., Kroncke, B. M., Law, C. L., Xia, Y., Droege, K. D., Van Horn, W. D., Vanoye, C. G., and Sanders, C. R. (2014) Purification and structural study of the

voltage-sensor domain of the human KCNQ1 potassium ion channel, *Biochemistry 53*, 2032-2042.
50. Chen, H., Pan, J., Gandhi, D. M., Dockendorff, C., Cui, Q., Chanda, B., and Henzler-Wildman, K. A. (2019) NMR Structural Analysis of Isolated Shaker Voltage-Sensing Domain in LPPG Micelles, *Biophys J 117*, 388-398.
51. Koehler, J., Sulistijo, E. S., Sakakura, M., Kim, H. J., Ellis, C. D., and Sanders, C. R. (2010) Lysophospholipid micelles sustain the stability and catalytic activity of diacylglycerol kinase in the absence of lipids, *Biochemistry 49*, 7089-7099.
52. Krueger-Koplin, R. D., Sorgen, P. L., Krueger-Koplin, S. T., Rivera-Torres, I. O., Cahill, S. M., Hicks, D. B., Grinius, L., Krulwich, T. A., and Girvin, M. E. (2004) An evaluation of detergents for NMR structural studies of membrane proteins, *J Biomol NMR 28*, 43-57.
53. Huang, H., Kuenze, G., Smith, J. A., Taylor, K. C., Duran, A. M., Hadziselimovic, A., Meiler, J., Vanoye, C. G., George, A. L., Jr., and Sanders, C. R. (2018) Mechanisms of KCNQ1 channel dysfunction in long QT syndrome involving voltage sensor domain mutations, *Sci Adv 4*, eaar2631.
54. Liang, B., Bushweller, J. H., and Tamm, L. K. (2006) Site-directed parallel spin-labeling and paramagnetic relaxation enhancement in structure determination of membrane proteins by solution NMR spectroscopy, *J Am Chem Soc 128*, 4389-4397.
55. Gottstein, D., Reckel, S., Dotsch, V., and Guntert, P. (2012) Requirements on paramagnetic relaxation enhancement data for membrane protein structure determination by NMR, *Structure 20*, 1019-1027.
56. Battiste, J. L., and Wagner, G. (2000) Utilization of site-directed spin labeling and high-resolution heteronuclear nuclear magnetic resonance for global fold determination of large proteins with limited nuclear overhauser effect data, *Biochemistry 39*, 5355-5365.
57. Ganguly, S., Weiner, B. E., and Meiler, J. (2011) Membrane protein structure determination using paramagnetic tags, *Structure 19*, 441-443.
58. Schwieters, C. D., Kuszewski, J. J., and Clore, G. M. (2006) Using XPLOR-NIH for NMR molecular structure determination., *Progress in Nuclear Magnetic Resonance Spectroscopy 48*, 47-62
59. Paramonov, A. S., Lyukmanova, E. N., Myshkin, M. Y., Shulepko, M. A., Kulbatskii, D. S., Petrosian, N. S., Chugunov, A. O., Dolgikh, D. A., Kirpichnikov, M. P., Arseniev, A. S., and Shenkarev, Z. O. (2017) NMR investigation of the isolated second voltage-sensing domain of human Nav1.4 channel, *Biochim Biophys Acta Biomembr 1859*, 493-506.
60. Zhou, H. X., and Cross, T. A. (2013) Influences of membrane mimetic environments on membrane protein structures, *Annu Rev Biophys 42*, 361-392.
61. Glauner, K. S., Mannuzzu, L. M., Gandhi, C. S., and Isacoff, E. Y. (1999) Spectroscopic mapping of voltage sensor movement in the Shaker potassium channel, *Nature 402*, 813-817.
62. Papazian, D. M., Shao, X. M., Seoh, S. A., Mock, A. F., Huang, Y., and Wainstock, D. H. (1995) Electrostatic interactions of S4 voltage sensor in Shaker K+ channel, *Neuron 14*, 1293-1301.
63. Tao, X., Lee, A., Limapichat, W., Dougherty, D. A., and MacKinnon, R. (2010) A gating charge transfer center in voltage sensors, *Science 328*, 67-73.

64. Lacroix, J. J., and Bezanilla, F. (2011) Control of a final gating charge transition by a hydrophobic residue in the S2 segment of a K+ channel voltage sensor, *Proc Natl Acad Sci U S A 108*, 6444-6449.
65. Restier, L., Cheng, L., and Sanguinetti, M. C. (2008) Mechanisms by which atrial fibrillation-associated mutations in the S1 domain of KCNQ1 slow deactivation of IKs channels, *J Physiol 586*, 4179-4191.
66. Chiamvimonvat, N., Chen-Izu, Y., Clancy, C. E., Deschenes, I., Dobrev, D., Heijman, J., Izu, L., Qu, Z., Ripplinger, C. M., Vandenberg, J. I., Weiss, J. N., Koren, G., Banyasz, T., Grandi, E., Sanguinetti, M. C., Bers, D. M., and Nerbonne, J. M. (2017) Potassium currents in the heart: functional roles in repolarization, arrhythmia and therapeutics, *J Physiol 595*, 2229-2252.
67. Keating, M. T., and Sanguinetti, M. C. (2001) Molecular and cellular mechanisms of cardiac arrhythmias, *Cell 104*, 569-580.
68. McCrossan, Z. A., and Abbott, G. W. (2004) The MinK-related peptides, *Neuropharmacology 47*, 787-821.
69. Kroncke, B. M., Van Horn, W. D., Smith, J., Kang, C., Welch, R. C., Song, Y., Nannemann, D. P., Taylor, K. C., Sisco, N. J., George, A. L., Jr., Meiler, J., Vanoye, C. G., and Sanders, C. R. (2016) Structural basis for KCNE3 modulation of potassium recycling in epithelia, *Sci Adv 2*, e1501228.
70. Preston, P., Wartosch, L., Gunzel, D., Fromm, M., Kongsuphol, P., Ousingsawat, J., Kunzelmann, K., Barhanin, J., Warth, R., and Jentsch, T. J. (2010) Disruption of the K+ channel beta-subunit KCNE3 reveals an important role in intestinal and tracheal Cl- transport, *J Biol Chem 285*, 7165-7175.
71. Barro-Soria, R., Perez, M. E., and Larsson, H. P. (2015) KCNE3 acts by promoting voltage sensor activation in KCNQ1, *Proc Natl Acad Sci U S A 112*, E7286-7292.
72. Barro-Soria, R., Ramentol, R., Liin, S. I., Perez, M. E., Kass, R. S., and Larsson, H. P. (2017) KCNE1 and KCNE3 modulate KCNQ1 channels by affecting different gating transitions, *Proc Natl Acad Sci U S A 114*, E7367-E7376.
73. Nakajo, K. (2019) Gating modulation of the KCNQ1 channel by KCNE proteins studied by voltage-clamp fluorometry, *Biophys Physicobiol 16*, 121-126.
74. Kuenze, G., Duran, A. M., Woods, H., Brewer, K. R., McDonald, E. F., Vanoye, C. G., George, A. L., Jr., Sanders, C. R., and Meiler, J. (2019) Upgraded molecular models of the human KCNQ1 potassium channel, *PLoS One 14*, e0220415.
75. Vanoye, C. G., Desai, R. R., Fabre, K. L., Gallagher, S. L., Potet, F., DeKeyser, J. M., Macaya, D., Meiler, J., Sanders, C. R., and George, A. L., Jr. (2018) High-Throughput Functional Evaluation of KCNQ1 Decrypts Variants of Unknown Significance, *Circ Genom Precis Med 11*, e002345.
76. DeCaen, P. G., Yarov-Yarovoy, V., Zhao, Y., Scheuer, T., and Catterall, W. A. (2008) Disulfide locking a sodium channel voltage sensor reveals ion pair formation during activation, *Proc Natl Acad Sci U S A 105*, 15142-15147.
77. Xu, X., Jiang, M., Hsu, K. L., Zhang, M., and Tseng, G. N. (2008) KCNQ1 and KCNE1 in the IKs channel complex make state-dependent contacts in their extracellular domains, *J Gen Physiol 131*, 589-603.
78. Lemak, A., Gutmanas, A., Chitayat, S., Karra, M., Fares, C., Sunnerhagen, M., and Arrowsmith, C. H. (2011) A novel strategy for NMR resonance assignment and protein structure determination, *J Biomol NMR 49*, 27-38.

79. Lee, W., Tonelli, M., and Markley, J. L. (2015) NMRFAM-SPARKY: enhanced software for biomolecular NMR spectroscopy, *Bioinformatics 31*, 1325-1327.
80. Kazimierczuk, K., and Orekhov, V. Y. (2011) Accelerated NMR spectroscopy by using compressed sensing, *Angew Chem Int Ed Engl 50*, 5556-5559.
81. Loria, J. P., Rance, M., and Palmer, A. G., 3rd. (1999) Transverse-relaxation-optimized (TROSY) gradient-enhanced triple-resonance NMR spectroscopy, *J Magn Reson 141*, 180-184.
82. Deatherage, C. L., Lu, Z., Kroncke, B. M., Ma, S., Smith, J. A., Voehler, M. W., McFeeters, R. L., and Sanders, C. R. (2017) Structural and biochemical differences between the Notch and the amyloid precursor protein transmembrane domains, *Sci Adv 3*, e1602794.
83. Wishart, D. S., and Sykes, B. D. (1994) The 13C chemical-shift index: a simple method for the identification of protein secondary structure using 13C chemical-shift data, *J Biomol NMR 4*, 171-180.
84. Shen, Y., and Bax, A. (2013) Protein backbone and sidechain torsion angles predicted from NMR chemical shifts using artificial neural networks, *J Biomol NMR 56*, 227-241.
85. Wu, E. L., Cheng, X., Jo, S., Rui, H., Song, K. C., Davila-Contreras, E. M., Qi, Y., Lee, J., Monje-Galvan, V., Venable, R. M., Klauda, J. B., and Im, W. (2014) CHARMM-GUI Membrane Builder toward realistic biological membrane simulations, *J Comput Chem 35*, 1997-2004.
86. Dickson, C. J., Madej, B. D., Skjevik, A. A., Betz, R. M., Teigen, K., Gould, I. R., and Walker, R. C. (2014) Lipid14: The Amber Lipid Force Field, *J Chem Theory Comput 10*, 865-879.
87. Case, D. A., Cheatham, T. E., 3rd, Darden, T., Gohlke, H., Luo, R., Merz, K. M., Jr., Onufriev, A., Simmerling, C., Wang, B., and Woods, R. J. (2005) The Amber biomolecular simulation programs, *J Comput Chem 26*, 1668-1688.

Figure Titles and Legends

Figure 1. NMR spectra of the human KCNQ1 voltage-sensor domain. (A) ^{1}H-^{15}N TROSY-HSQC spectrum recorded at 900 MHz of ^{2}H,^{13}C,^{15}N-Q1-VSD in LMPG micelles. Backbone amide peaks for 140 out of 147 non-proline residues (95%) have been assigned. Only a single set of peaks is observed. **(B)** ^{1}H-^{13}C HSQC methyl optimized spectrum recorded at 900 MHz of ^{13}C,^{15}N-Q1-VSD in perdeuterated LMPG micelles. Methyl groups for 58 out of 68 (85%) residues were assigned (Ala 10 of10, Thr 6 of 8, Ile 9 of 11, Val 18 of 22, Leu 15 of 17). In addition to the presence of a very limited number of unassigned peaks from the VSD in this spectrum other unassigned peaks likely derive from natural abundance ^{13}C in residually-protonated LMPG and also from the fully protonated buffer components TCEP and MES. The chemical shift assignments illustrated for panels A and B shift have been deposited in BioMagResBank (BMRB ID 30517).

Figure 2. **Structure of the KCNQ1 VSD. (A)** The human KCNQ1 VSD NMR-determined ensemble after molecular dynamics refinement in a hydrated DMPC bilayer (PDB ID 6MIE, see statistics in Table 1 and also Figure 2-figure supplement 1) **(B)** Cryo-EM structure of the *Xenopus* KCNQ1 VSD (PDB ID 5VMS)[22]. **(C)** Representative low energy NMR structure from PDB 6MIE. In panels A-C, the transmembrane helices S1, S2, S3, and S4, are colored bluish green, yellow, vermillion, and sky blue respectively. The S2-S3 linker and S0 helices are colored reddish purple and orange. The approximate position of the membrane-water interfaces is indicated by a pair of black lines in panels A and B.

Figure 3. Comparison of intermediate and activated KCNQ1 VSD conformations. (A) Intermediate conformation of human KCNQ1 VSD (1st structure in the PDB 6MIE ensemble). **(B)**

Activated conformation of the *Xenopus* KCNQ1 VSD (PDB 5VMS)[22]. In both panels the Cα atoms of the S4 polar residues are shown as yellow spheres and the transmembrane helices are labeled in vermillion text. S0 and S1 are not shown to improve clarity of side chain interactions. **(C)** Overlay of the NMR (sky blue) and cryoEM (bluish green) structures of the KCNQ1 VSD. All structural elements other than the S4 helix are semi-transparent. The Cα of the human residue G229 and the corresponding *Xenopus* residue G219 are shown as spheres. (**D**) Sequence alignments for S2 and S4 in the KCNQ/Kv7 family and select other voltage-gated ion channels.

Figure 4. S2-S4 salt bridges/hydrogen bonds in the NMR- and cryoEM-structures of the KCNQ1 VSD. (A) Intermediate state conformation of human KCNQ1 VSD (1st structure in the PDB 6MIE ensemble). Of particular note are the ionic interactions of E1-R2 and E2-R4, as well as, the close packing of Q3 and F0. **(B)** Activated state conformation of the *Xenopus* KCNQ1 VSD (PDB 5VMS). Note the gating charge residue pairings of E1-R4 and H5-E2. In all panels the Cα atoms of the S4 polar residues are shown as yellow spheres and the transmembrane helices are labeled in vermillion text. S0 and S1 are not shown to improve clarity of side chain interactions.

Figure 5. Schematics and electrophysiology data validating the intermediate and activated KCNQ1 VSD functional states utilizing auxiliary subunit KCNE1 regulation as a probe. Amino acid residue nomenclature: E2 = E170, R4 = R237, F0 = F167, Q3 = Q234, and H5 = H240. Numbering corresponds to the human KCNQ1 sequence. All error bars are ±SEM. All horizontal scale bars correspond to 2 seconds. **(A)** A cartoon schematic illustrating key S2, S3, and S4 residues interactions found in the NMR and cryoEM VSD structures. Positive and polar gating residues on S4 (R1-H5) are colored blue, negative counter charges on S2 (E1, E2)

and S3 (D202) are colored red, and the hydrophobic plug on S2 (F0) is colored orange. **(B)** A cartoon schematic displaying how the S4 charge-reversal mutation (Q3E) disrupts VSD function. Q3E mutation creates electrostatic repulsion with the negative counter charges (E1, E2) and leads to VSD loss of function. **(C)** A cartoon schematic showing how the double charge-reversal mutations Q3E/F0R biases VSD conformation. The double mutations ensure that electrostatic interactions between S2 and S4 are only favorable when the two mutation sites are in alignment (Q3E-F0R). **(D)** Table detailing KCNE1 effect on the KCNQ1 pore domain associated with the intermediate or activated VSD states based on prior studies. KCNE1 suppresses the IO state current by decrease open probability, while enhancing the AO state current, in part by increasing unitary conductance[11,12,19]. **(E)** Representative current recordings from the KCNQ1 channel without (left) and with (right) KCNE1 co-expression. The voltage protocol is shown in the inset and applies to all exemplars in this figure. **(F-H)** Left: Cartoon schematic of the double-charge reversal mutation and the predicted S2-S4 registry for the mutant tested. Middle: Exemplar currents for the mutant recorded with and without KCNE1 co-expression. Right: Average steady-state current vs. voltage (IV) curves for the respective mutants in the absence or presence of KCNE1 co-expression. The inset in panel E shows the voltage protocol. n = 5 (F), 5 (G), 6 (H). Currents were collected with 10 mV interval, but examples are shown with 20 mV interval for clarity.

Figure 6. Electrophysiology validating the intermediate and activated KCNQ1 VSD functional states utilizing XE991 pharmacology as a probe. Amino acid residue nomenclature and numbering and error bars are similar as in Figure 5. **(A)** Table outlining 5 µM XE991 effect on KCNQ1 IO and AO state currents based on prior studies[11]. **(B)** Top: Exemplar diary plots of E2R/R4E drug studies demonstrating current amplitude over time. Cells were held at -20 mV and pulsed to +40 mV for 4 seconds and -40 mV for 2 seconds every 20 seconds.

Each dot plots the steady-state current amplitude at the end of the 4-seconds +40 mV test pulse. Cells were recorded in ND96 solution and the top bars indicate application of 5 μM XE991 (red) and 150 μM chromanol 293B (blue). Scale bar indicates 5 minutes. Bottom: Current traces for the E2R/R4E mutant in control ND96 solution (black), in solution containing 5 μM XE991 (red), and in solution containing 150 μM chromanol 293B (blue). The arrows in the diary plot indicate respective traces shown. Note that because the holding potential was -20 mV and the mutant channels are constitutively open, non-zero currents were observed before the test pulse. **(C)** Chromanol-subtracted E2R/R4E currents under control (black) and 5 μM XE991 (red) conditions for the traces shown in panel B. The chromanol-subtracted currents were calculated by subtracting current after chromanol application (blue, panel B) from the control current (black, panel B) and the current after XE991 application (red, panel B). Percent E2R/R4E current inhibition by XE991 was calculated from the chromanol-subtracted currents using the ratio between the steady-state current amplitude under XE991 and control conditions (see Methods). **(D)** Average percent inhibition of the E2R/R4E currents by 5 μM XE991, as quantified by the chromanol-subtracted currents (n = 6). Error bar indicates SEM and applies to all error bars in this figure. **(E-J)** Same as panels B-D, but showing results for KCNQ1 F0R/Q3E/D202N and F0R/H5E/D202N mutants (n = 6 for both mutants).

Figure 7. KCNE3 shifts the voltage dependence of the intermediate-open state to render its conductance relevant under physiological conditions. (A) Voltage-clamp fluorometry recordings for pseudo-WT (C214A/G219C/C331A) KCNQ1 (left), KCNQ1+KCNE1 (middle), and KCNQ1+KCNE3 (right). Current (black) and fluorescence (blue) were recorded with voltages from -160 mV to +100 mV in 20 mV increments and then back to -40 mV. The bottom panels are the G–V (black) and F–V (blue) relationships with F_1 and F_2 components (dotted lines). The F–V relationship for KCNQ1 (gray) is also shown in KCNQ1+KCNE1 and KCNQ1+KCNE3 for

comparison. **(B)** VCF recordings for KCNQ1-F351A in the presence (blue) and absence (gray) of KCNE3. The bottom of this panel shows the G–V and F–V relationships for KCNQ1-F351A (gray) and KCNQ1-F351A+KCNE3 (blue). **(C)** Left: WT KCNQ1+KCNE3 currents (black) with voltages from -120 mV to +80 mV in 20 mV increments and back to -40 mV to test the tail current. The red traces are total KCNQ1+KCNE3 currents with the instantaneous current subtracted, which show typical time- and voltage-dependent activation. Right: The two steps of KCNQ1+KCNE3 voltage sensor activation, F_1 and $F_{2,}$ are shown in blue, while transitions of the two conductive states are shown in black (GV_1) and red (GV_2). **(D)** Overlays of stabilized currents in control solutions (black traces for all channels) and after applying 5 μM XE991 for KCNQ1 (grey), KCNQ1+KCNE1 (blue), and KCNQ1+KCNE3 (red). **(E)** Time-dependent inhibition of 5 μM XE991 of KCNQ1 (black), KCNQ1+KCNE1 (blue), and KCNQ1+KCNE3 (red). Time-dependent inhibition was calculated by dividing the stabilized currents in solutions containing 5 μM XE991 by that of control at the same time point. X-axis is the time after the start of the +40 mV test pulse. In all cases, n ≥ 3.

Figure Supplements: Titles and Legends

Figure 1-figure supplement 1. Long range PREs are consistent with the expected KCNQ1 VSD topology in LMPG micelles. The residue positions of the spin-labeled cysteines for each sample are : (**A**) 144-SL (**B**) 155-SL (**C**) 214-SL (**D**) 224-Sl (**E**) 121-SL (**F**) 177-Sl (**G**) 180-SL (**H**) 238-SL.

Figure 1-figure supplement 2. TALOS-N secondary structure analysis of backbone chemical shifts (top panel) and (bottom panels) deviations of the $^{13}C\alpha$ and carbonyl $^{13}C'$

chemical shifts from random coil values. The chemical shift data for the KCNQ1 VSD been deposited in BioMagResBank (BMRB ID 30517).

Figure 1-figure supplement 3. Examples of NOE measurements. Example strip plots showing long-range methyl-methyl and methyl-backbone Hα proton NOEs (red arrows) taken from the methyl-optimized 3D ^{13}C-edited NOESY recorded on a ^{13}C,^{15}N-labeled sample in deuterated LMPG. The chemical shift assignments illustrated in this figure have been deposited in BioMagResBank (BMRB ID 30517).

Figure 2-figure supplement 1. KCNQ1-VSD XplorNIH-determined structural ensemble, before and after molecular dynamics refinement. **(A)** The ensemble is comprised of the top 15 lowest energy structures out of 150 conformations generated by NMR data-restrained XplorNIH calculations (no bilayer). The transmembrane helices S1, S2, S3, and S4, are colored bluish green, yellow, vermillion, and sky blue respectively. The S2-S3 linker and S0 helices are colored orange and reddish purple. The loop between S1 (bluish green) and S2 (yellow) appears disordered due to lack of NMR-derived restraints. This does not necessarily mean this region does not adopt stable secondary structure. The approximate position of the membrane is indicated by a pair of grey lines. **(B)** The unrestrained molecular dynamics refined ensemble (MD carried out in an explicit hydrated DMPC bilayer) colored as in panel A (corresponding to PDB ID 6MIE containing 10 conformers). **(C)** The upper panel shows the total number of distance restraints per residue. For NOE-derived restraints that define a distance between two atoms in different residues, each residue receives a count of 0.5 per restraint. Long range, medium, and sequence distance restraints are colored red, black, and light grey respectively. For PRE-derived restraints, which define the distance between a given backbone amide and the

MTSL free radical of the spin labeled residue, a count of 1.0 is added to the non-labeled residue. PRE-derived restraints are colored dark grey. The lower panel plots the backbone r.m.s.d. vs. residue number for the Xplor-NIH ensemble. The helical sections of secondary structure are indicated with colored boxes corresponding to the cartoon representation. **(D)** The backbone r.m.s.d. to seed starting coordinates of the transmembrane helices (red) and all residues (black) over the course of the unrestrained trajectory is shown.

Figure 5-figure supplement 1. Electrophysiology results for KCNQ1 F0R single and double mutants with and without KCNE1 co-expression, and with XE991 exposure. F0 = F167; Q3 = Q234; R4 = R237; H5 = H240. Residue numbers correspond to human KCNQ1. All error bars are ±SEM. **(A)**Top: Current recordings of KCNQ1 F0R single mutant with and without KCNE1 co-expression. Bottom: Average GV relationships for KCNQ1 F0R (black, n = 3), KCNQ1 F0R + KCNE1 (dark blue, n = 5), KCNQ1 WT (gray), and KCNQ1 WT + KCNE1 (light blue). The single mutant KCNQ1 F0R exhibited dramatic left-shifted voltage-dependent activation compared to KCNQ1 WT, suggesting that the mutation destabilizes the resting state VSD. KCNE1 co-expression restored voltage-dependent activation to near WT levels and potentiated ionic current compared to the α-subunit alone, suggesting that KCNE1 partly rescues the ability of the single mutant F0R to gate normally. **(B-E)** Top: Current recordings of KCNQ1 F0R double mutants with and without KCNE1 co-expression. Bottom: Average GV relationships for the KCNQ1 double mutant α-subunit only (black), KCNQ1 double mutant + KCNE1 (dark blue), KCNQ1 F0R (grey), and KCNQ1 F0R + KCNE1 (light blue). All n > 3. **(B)** F0R/D202N featured a further left-shifted voltage-dependent activation compared to F0R single mutant. KCNE1 co-expression greatly suppressed F0R/D202N current, suggesting that F0R/D202N favored the intermediate VSD state and IO channel state. **(C)** F0R/Q3E demonstrated current suppression upon KCNE1 co-expression when compared to α-subunit

alone, suggesting that F0R/Q3E favored the intermediate VSD state and the IO channel state. Furthermore, the conductance-voltage (G-V) curve for the mutant KCNQ1 co-expressed with KCNE1 tracks the development of the AO state because KCNE1 suppresses IO-state current. F0R/Q3E+KCNE1 featured a right-shifted voltage-dependent activation compared to F0R single mutant, consistent with the mutant favoring the intermediate VSD state and resisting transition into the AO state. **(D-E)** F0R/R4E and F0R/H5E double mutants exhibited an opposite phenotype compared to F0R/Q3E. Upon KCNE1 co-expression, ionic currents for F0R/R4E and F0R/H5E were potentiated, and voltage-dependent activation was left-shifted compared to the F0R single mutant. Together, these results suggest F0R/R4E and F0R/H5E favored the activated VSD state and the AO state. Overall, F0R/Q3E and F0R/D202N double mutants demonstrated phenotypes consistent with the mutants favoring the IO channel state; while F0R/R4E and F0R/H5E exhibited distinct and opposite phenotypes, suggesting that the latter mutants promote the AO channel state. However, the presence of voltage-dependence in these mutants represents a confounding factor, as the VSD retain voltage sensitivity. By adding the S3 D202N mutation into the F0R/Q3E and F0R/H5E mutants, this voltage-dependence was abolished (Main Figure 5), suggesting that the triple mutants highly stabilize the VSD states and that the charge transfer residue S3 D202 plays a role in maintaining the voltage-dependence of the mutants F0R/Q3E and F0R/H5E. Importantly, F0R/Q3E/D202N and F0R/H5E/D202N demonstrated qualitatively identical phenotypes compared to F0R/Q3E and F0R/H5E (Main Figure 5), but without the confounding factor of voltage-dependence. **(F-J)** Steady-state current recordings of KCNQ1 mutants in control ND96 solution (black), 5 μM XE991 solution (red), and 150 μM chromanol 293B solution (blue). Note that the holding potential was -20 mV as shown by the inset voltage protocols. The -20 mV holding potential yielded non-zero currents before the test pulse because the mutants were constitutively opened. Bar plots show average chromanol-sensitive current inhibition (see Methods). All n > 3. Mutants F0R/D202N and

F0R/Q3E demonstrated robust and characteristic IO-current inhibition by 5 μM XE991, consistent with the idea that F0R/D202N and F0R/Q3E favor the IO state. In contrast, mutants F0R, F0R/R4E, and F0R/H5E featured the characteristic AO-current insensitivity to 5 μM XE991, consistent with the hypothesis that these mutations promote the AO state. Critically, XE991 data provided consistent categorization of the F0R single and double mutants when compared to KCNE1 co-expression data (panels A-E), lending further support to the conclusion that these mutants can be classified as promoting the IO state (F0R/D202N, F0R/Q3E) or the AO state (F0R/R4E, F0R/H5E).

Source Data Files

Figure 5-source data Excel file with numerical data used for Figure 5.

Figure 6-source data Excel file with numerical data used for Figure 6.

Figure 7-source data Excel file with numerical data used for Figure 7.

Figure 1-figure supplement 1 source data Excel file with numerical data used for Figure 1-figure supplement 1.

Figure 1-figure supplement 2 source data Excel file with numerical data used for Figure 1-figure supplement 2.

Figure 2-figure supplement 1 source data 1 Text file with coordinates (PDB format) of the XPLOR-NIH structure ensemble for the KCNQ1-VSD prior to molecular dynamics.

Figure 2-figure supplement 1, source data 2 Excel file with numerical data used for Figure 2-figure supplement 1C, top panel.

Figure 2-figure supplement 1, source data 3 Excel file with numerical data used for Figure 2-figure supplement 1C, bottom panel.

Figure 2-figure supplement 1, source data 4 Excel file with numerical data used for Figure 2-figure supplement 1D, top panel.

Figure 5-figure supplement 1 source data Excel file with numerical data used for Figure 5-figure supplement 1.

Figure 5-figure supplement 1 source code MATLAB script that takes in tail current data obtained from PatchMaster program (see Resources Table), fits the data with a Boltzmann equation, and outputs the best fit parameters.

Table 1. KCNQ1 VSD NMR structure statistics.

Structure restraints	**XplorNIH[a]**	**PDB 6MIE[b]**
Total NOE	958	
Inter-residue		
Sequential (| i - j | = 1)	559	
Medium-range (1 < | i - j | < 5)	366	
Long-range (| i - j | ≥ 5)	33	
Hydrogen bonds[c]	55	
Paramagnetic relaxation enhancement	403	
Dihedral angle		
ϕ	97	
φ	97	
Residual dipolar couplings ($^1D_{HN}$)	54	
Structure statistics		
Ensemble r.m.s.d. (residues 120-152, 160-239)		
Backbone heavy atoms (Å)	1.41	0.96
All heavy atoms (Å)	2.33	1.72
Transmembrane r.m.s.d. (residues 120-142, 160-179, 198-215, 219-239)		
Backbone heavy atoms (Å)	0.87	0.97
r.m.s.d. from experimental restraints		
Distances (Å)	0.068 ± 0.005	0.150 ± 0.019
Dihedral angles (°)	1.0 ± 0.2	10.3 ± 4.2
Residual dipolar coupling (Hz)	0.92 ± 0.21	3.1 ± 0.6
r.m.s.d. from idealized geometry		
Bond lengths (Å)	0.003 ± 0.001	0.005 ± 0.001
Bond Angles (°)	0.44 ± 0.01	1.71 ± 0.01
Ramachandran plot (residues 101-152, 160-239)[c]		
Most favorable (%)	89.3 ± 2.0	89.8 ± 2.8
Additionally allowed (%)	10.0 ± 2.2	8.8 ± 2.3
Generously allowed (%)	0.4 ± 0.8	0.7 ± 0.6
Disallowed (%)	0.3 ± 0.8	0.6 ± 0.7

[a]"XplorNIH" describes the statistics for the XplorNIH structure ensemble generated using experimental restraints, prior to the rMD phase of the calculations.
[b]"MD" describes the statistics for the structure ensemble (PDB ID: 6MIE) (see Methods).
[c]Procheck NMR

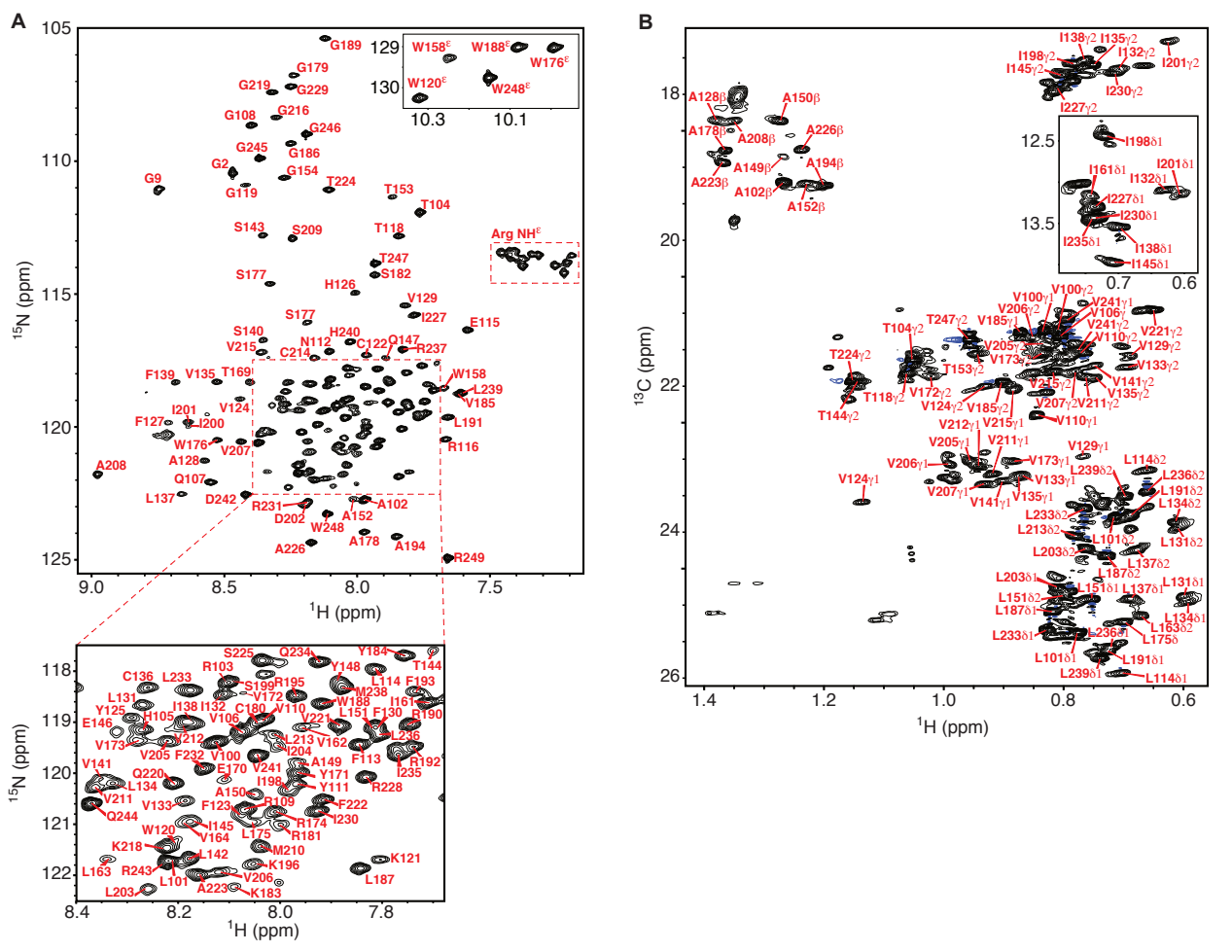
A
B
^{15}N (ppm)
^{1}H (ppm)
^{13}C (ppm)
Arg NH$^{\varepsilon}$
W158$^{\varepsilon}$
W188$^{\varepsilon}$
W176$^{\varepsilon}$
W120$^{\varepsilon}$
W248$^{\varepsilon}$

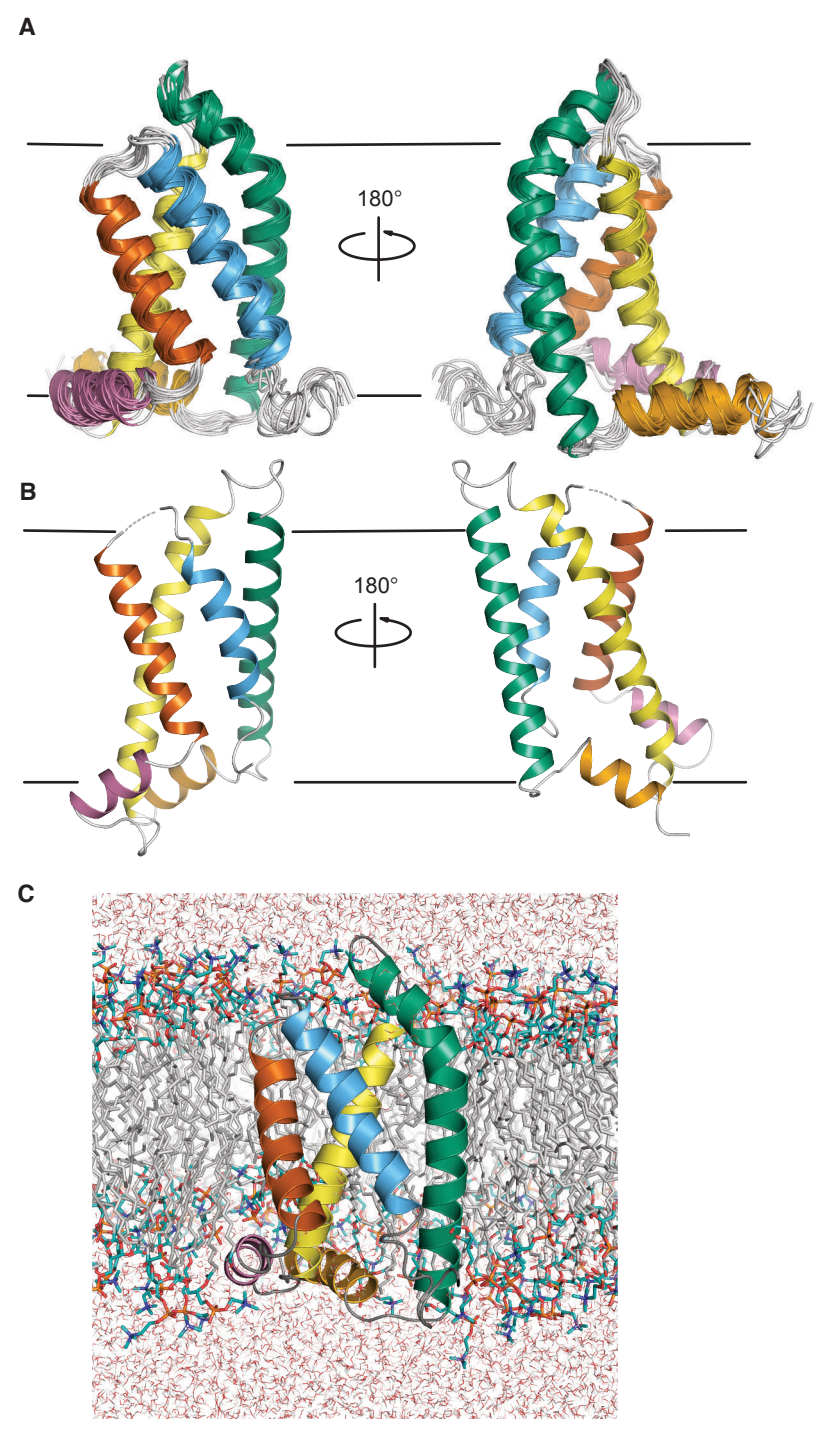
A
180°
B
180°
C

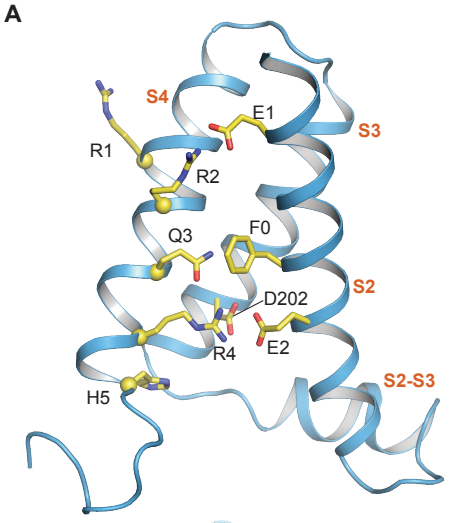

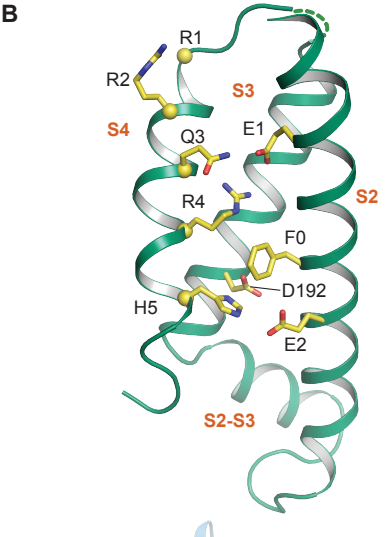

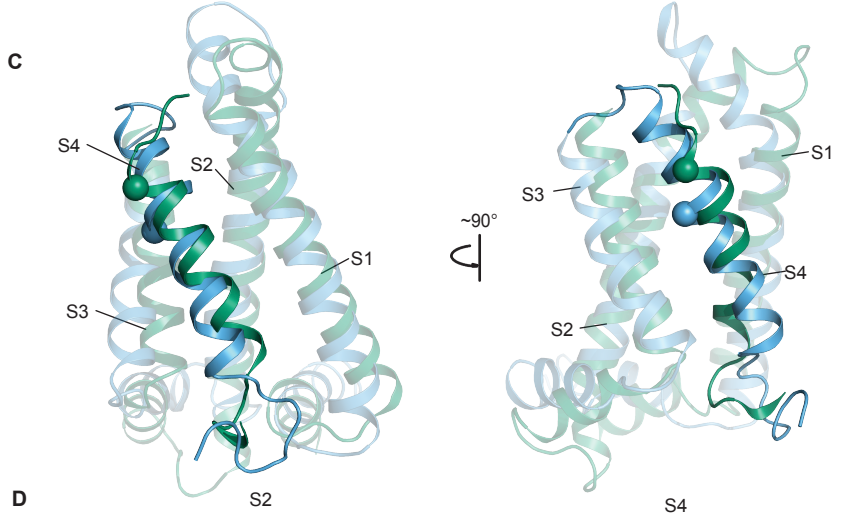

D

S2 S4

E1 F0 E2 R1 R2 Q3 R4 H5 R6

```
hKv7.1   155-TLFWMEIVLVVFFGTEYVVRLWS-177  223-ATSAIRGIRFLQILRML-H-VDRQGG-246
fKv7.1       TLFWMEIVLVVFFGAEYVVRLWS      ATSAIRGIRFLQILRML-H-VDRQGG
hKv7.2       ALYILEIVTIVVFGVEYFVRIWA      ATSALRSLRFLQILRMI-R-MDRRGG
hKv7.3       WLLLLETFAIFIFGAEFALRIWA      ATS-LRSLRFLQILRML-R-MDRRGG
hKv7.4       CLLILEFVMIVVFGLEYIVRVWS      ATSALRSMRFLQILRMV-R-MDRRGG
hKv7.5       CLLILEFVMIVVFGLEFIIRIWS      ATSALRSLRFLQILRMV-R-MDRRGG
Kv1.2        PFFIVETLCIIWFSFEFLVRFFA      SLAILRVIRLVRVFRIF-K-LSRHSK
Kv10.1       AWLVVDSIVDVIFLVDIVLNFHT      LFSSLKVVRLLRLGRVA-RKLDHYIE
Shaker       PFFLIETLCIIWFTFELTVRFLA      SLAILRVIRLVRVFRIF-K-LSRHSK
Nav1.5       WTKYVEYTFTAIYTFESLVKILA      NVSALRTFRVLRALKTI-S-VISGLK
KvAP         RLYLVDLILVIILWADYAYRAYK      ---LFRLVRLLRFLRILLI-ISRGSK
Cav1.1       GLEKLEYFFLIVFSIEAAMKIIA      DVKALRAFRVLRPLRLV-S-GVPSLQ
```

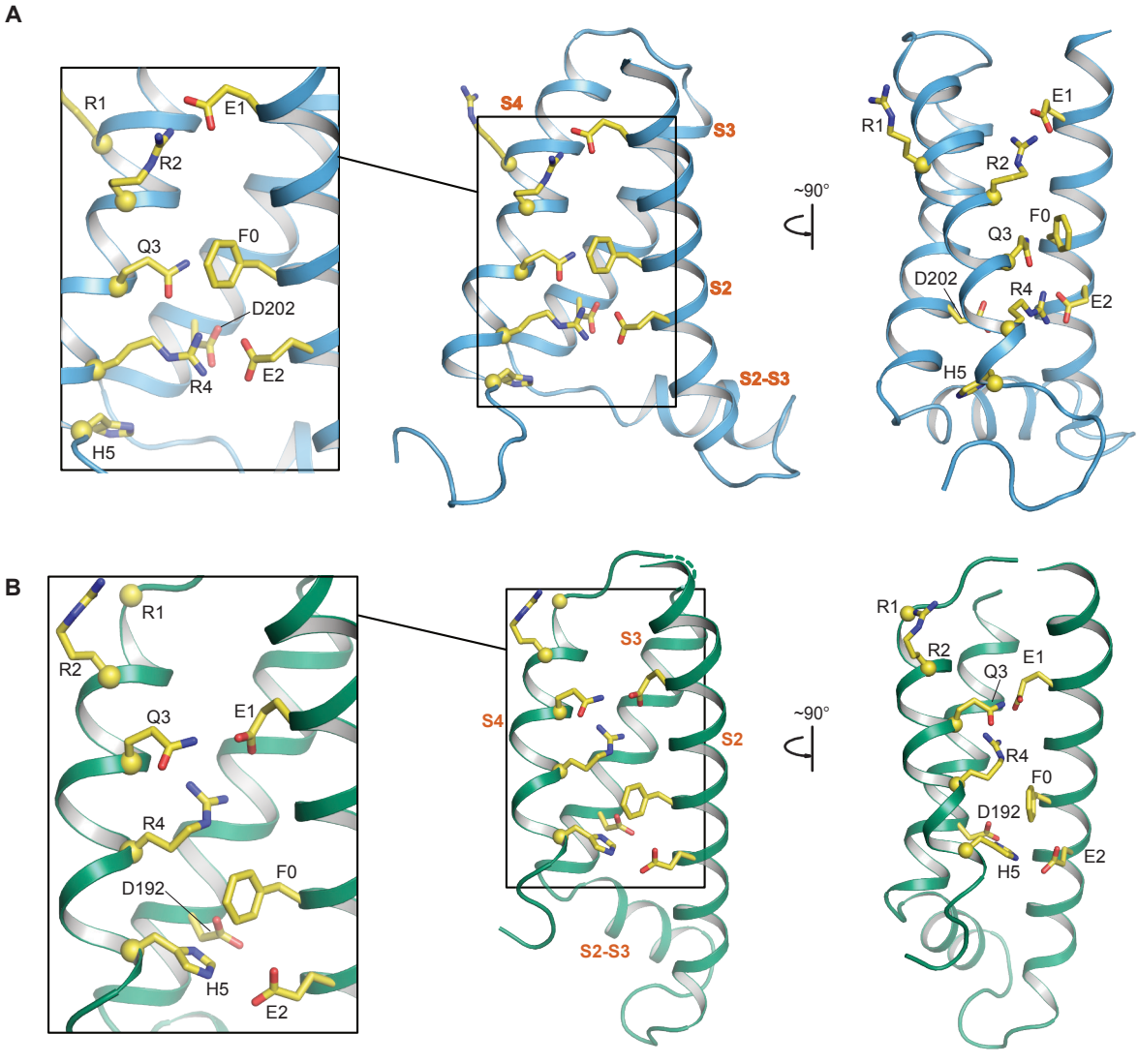
A
R1
E1
R2
Q3
F0
D202
R4
E2
H5
S4
S3
S2
S2-S3
~90°
R1
E1
R2
F0
Q3
D202
R4
E2
H5
B
R1
R2
Q3
E1
R4
F0
D192
H5
E2
S4
S3
S2
S2-S3
~90°
R1
R2
E1
Q3
R4
F0
D192
H5
E2

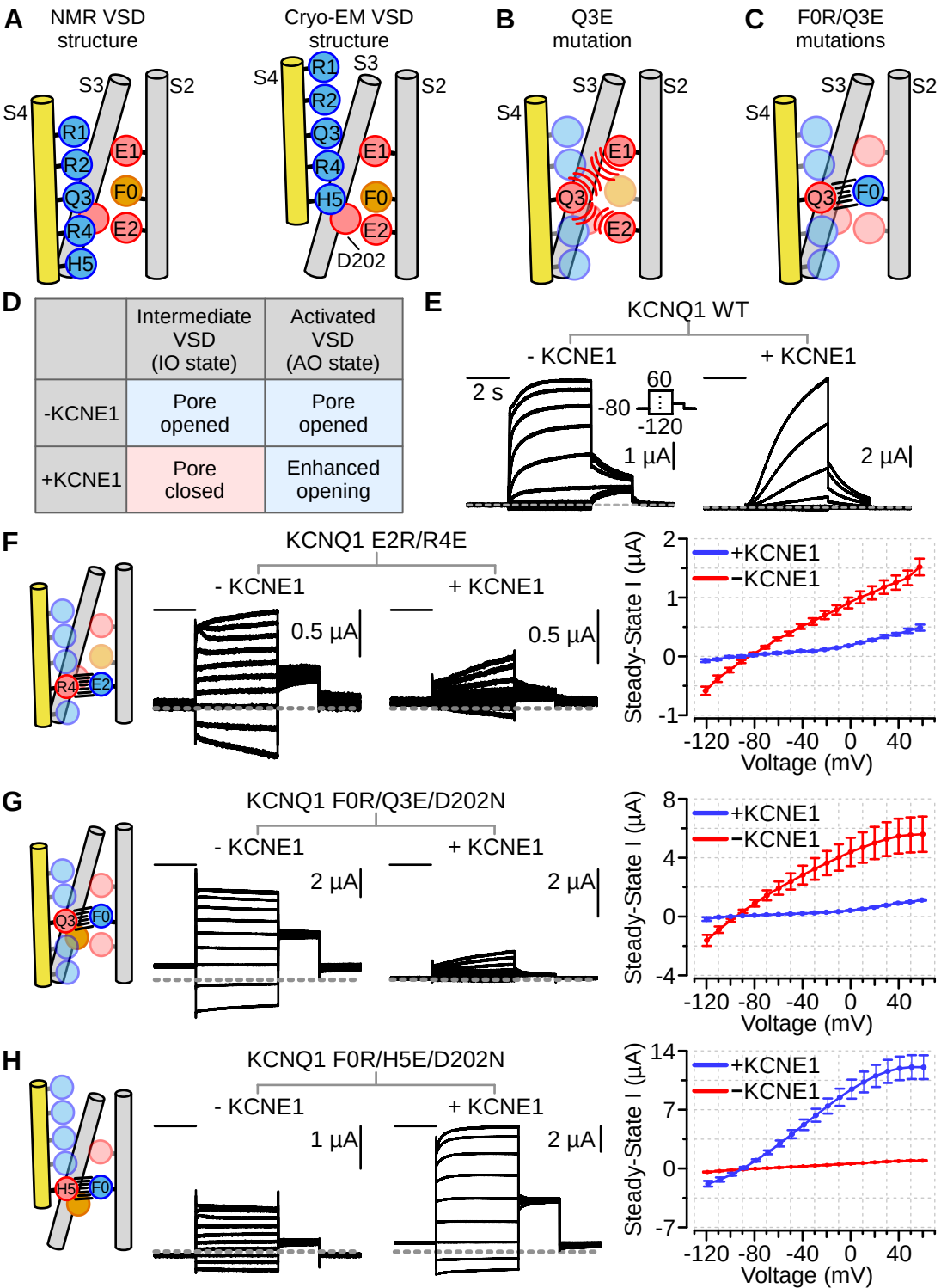
A
NMR VSD structure
Cryo-EM VSD structure
S3
S2
S4
R1
R2
Q3
R4
H5
E1
F0
E2
D202
B
Q3E mutation
C
F0R/Q3E mutations
D
Intermediate VSD (IO state)
Activated VSD (AO state)
-KCNE1
Pore opened
Pore opened
+KCNE1
Pore closed
Enhanced opening
E
KCNQ1 WT
- KCNE1
+ KCNE1
2 s
60
-80
-120
1 μA
2 μA
F
KCNQ1 E2R/R4E
0.5 μA
G
KCNQ1 F0R/Q3E/D202N
H
KCNQ1 F0R/H5E/D202N
Steady-State I (μA)
Voltage (mV)
+KCNE1
−KCNE1

A

	Intermediate VSD (IO state)	Activated VSD (AO state)
+5μM XE991	Strongly inhibited	Weakly inhibited

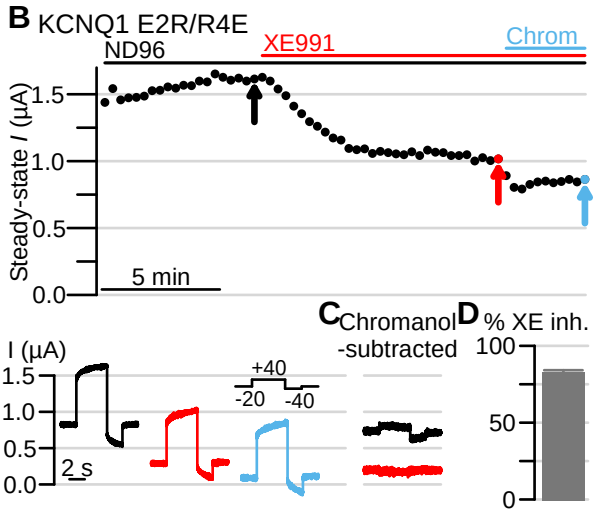

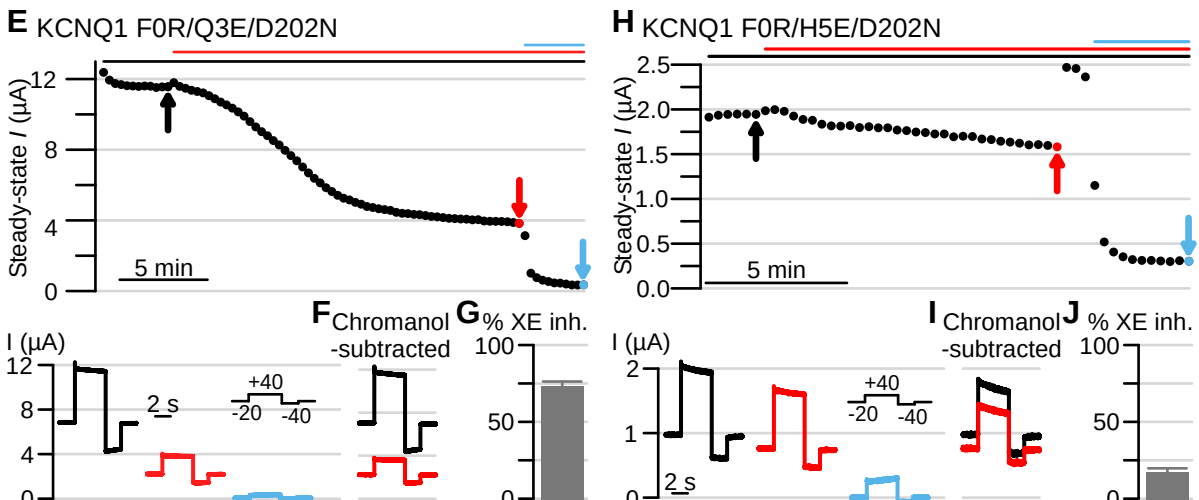

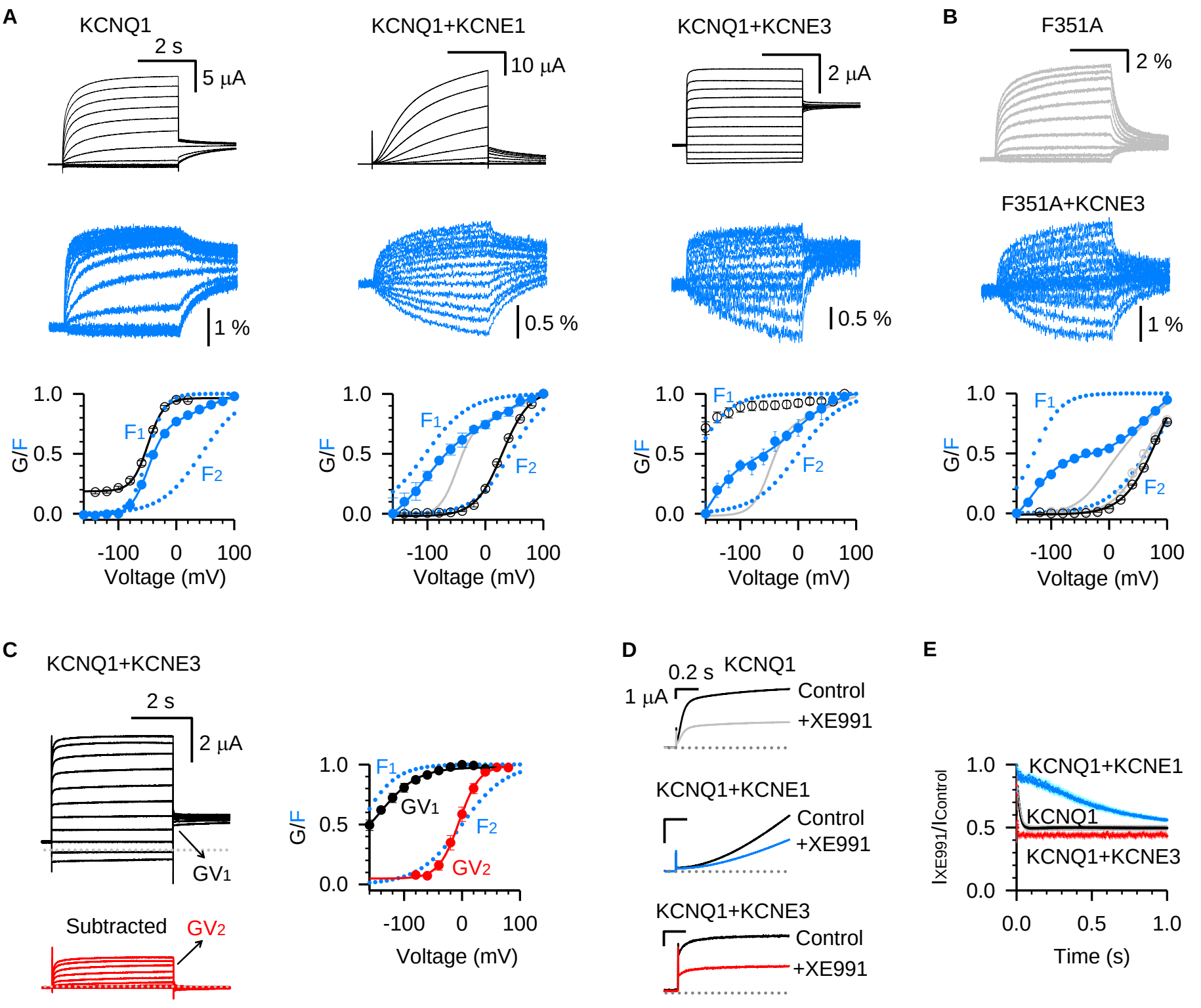
A
KCNQ1
2 s
5 µA
1 %
KCNQ1+KCNE1
10 µA
0.5 %
KCNQ1+KCNE3
2 µA
0.5 %
G/F
F1
F2
Voltage (mV)
B
F351A
2 %
F351A+KCNE3
1 %
C
KCNQ1+KCNE3
2 s
2 µA
GV1
Subtracted
GV2
D
KCNQ1
0.2 s
1 µA
Control
+XE991
KCNQ1+KCNE1
KCNQ1+KCNE3
E
IXE991/IControl
KCNQ1+KCNE1
KCNQ1
KCNQ1+KCNE3
Time (s)

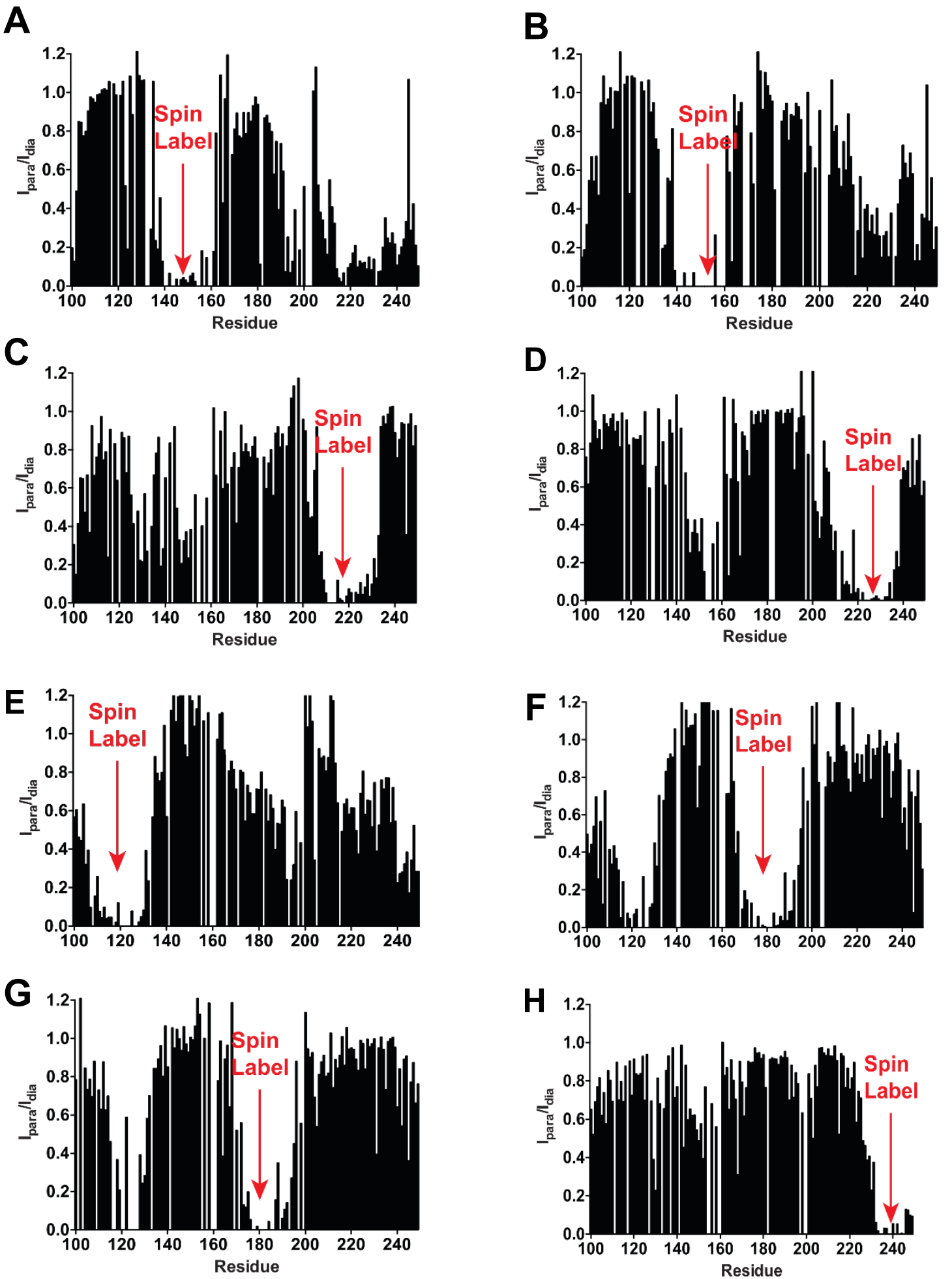
A
B
C
D
E
F
G
H
Spin Label
I_{para}/I_{dia}
Residue
0.0
0.2
0.4
0.6
0.8
1.0
1.2
100
120
140
160
180
200
220
240

S0 S1 S2 linker S3 S4

MGHHHHHHGVLARTHVQGRVYNFLERPTGWKCFVYHFAVFLIVLVCLIFSVLSTIEQYAALATGTLFWMEIVLVVFFGTEYVVRLWSAGCRSKYVGLWGRLRFARKPISIIDLIVVVASMVVLCVGSKGQVFATSAIRGIRFLQILRMLHVDRQGGTWR

α-Helix

1.0

0.5

0.0

$\Delta\delta^{13}C\alpha$ (ppm)

6

4

2

0

-2

$\Delta\delta^{13}C'$ (ppm)

4

2

0

-2

120 140 160 180 200 220 240

Residue Number

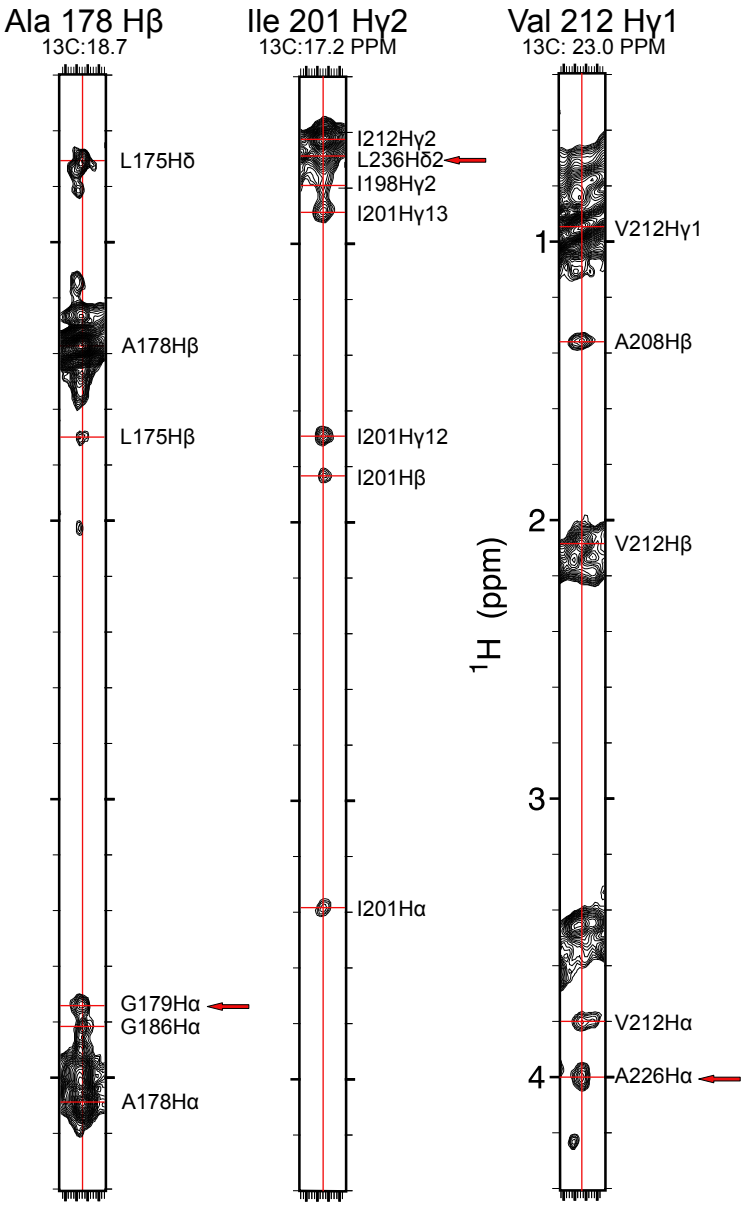
Ala 178 Hβ
13C:18.7
L175Hδ
A178Hβ
L175Hβ
G179Hα
G186Hα
A178Hα
Ile 201 Hγ2
13C:17.2 PPM
I212Hγ2
L236Hδ2
I198Hγ2
I201Hγ13
I201Hγ12
I201Hβ
I201Hα
Val 212 Hγ1
13C: 23.0 PPM
V212Hγ1
A208Hβ
V212Hβ
V212Hα
A226Hα
1
2
3
4
1H (ppm)

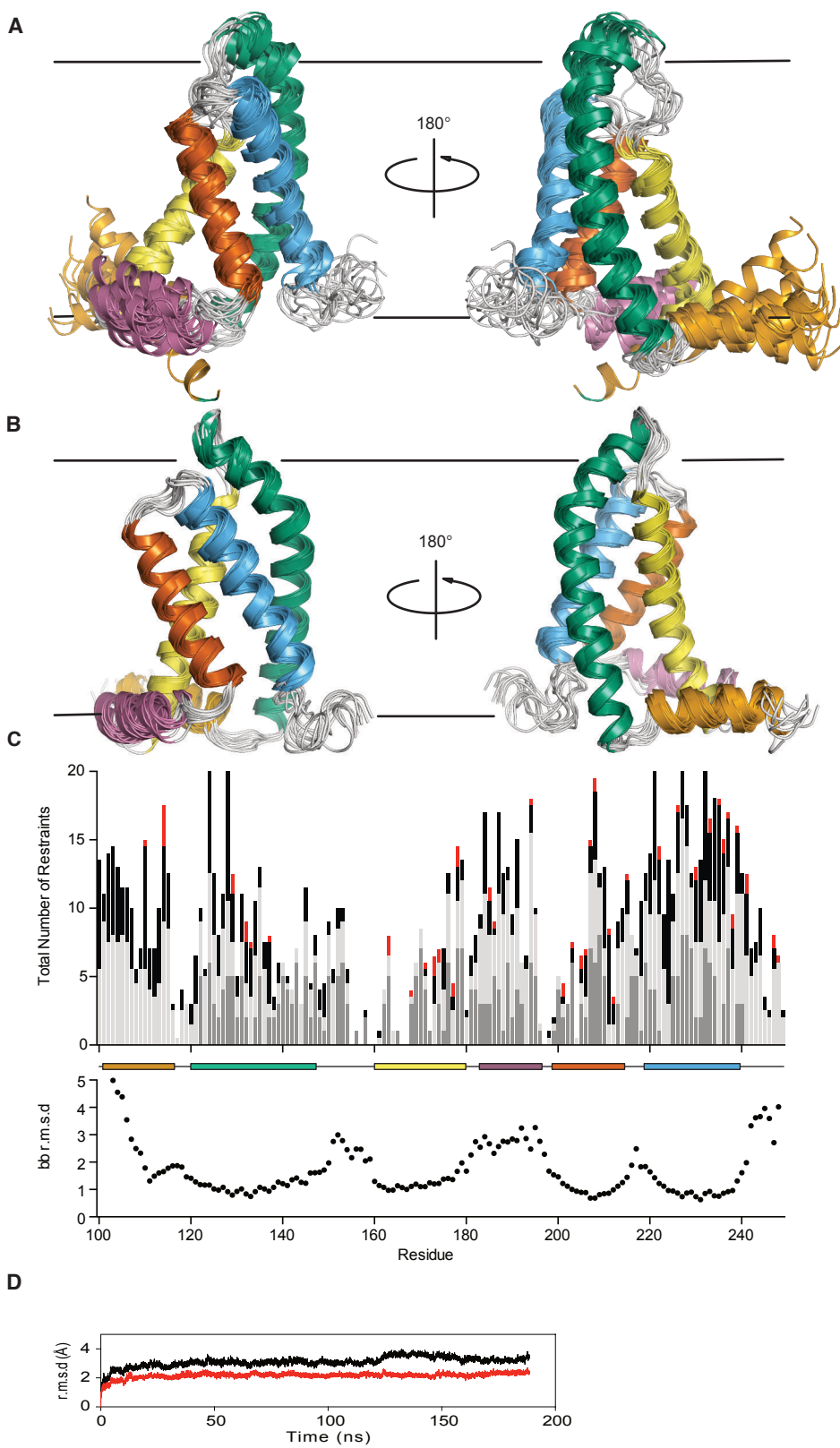
A
180°
B
180°
C
Total Number of Restraints
20
15
10
5
0
bb r.m.s.d
5
4
3
2
1
0
100
120
140
160
180
200
220
240
Residue
D
r.m.s.d (Å)
4
2
0
0
50
100
150
200
Time (ns)

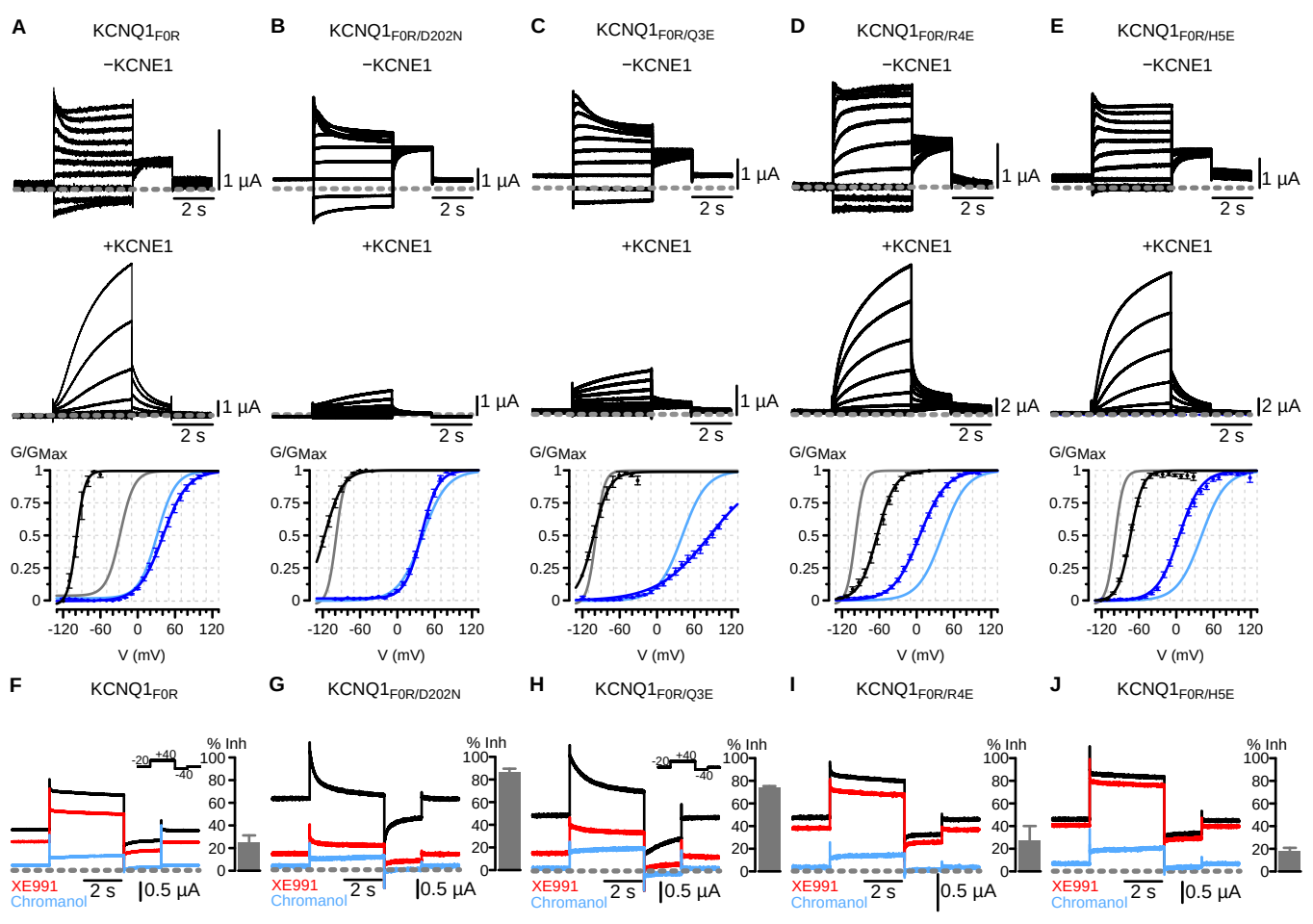
A
KCNQ1F0R
−KCNE1
1 µA
2 s
+KCNE1
1 µA
2 s
G/GMax
1
0.75
0.5
0.25
0
-120 -60 0 60 120
V (mV)
B
KCNQ1F0R/D202N
−KCNE1
1 µA
2 s
+KCNE1
1 µA
2 s
G/GMax
1
0.75
0.5
0.25
0
-120 -60 0 60 120
V (mV)
C
KCNQ1F0R/Q3E
−KCNE1
1 µA
2 s
+KCNE1
1 µA
2 s
G/GMax
1
0.75
0.5
0.25
0
-120 -60 0 60 120
V (mV)
D
KCNQ1F0R/R4E
−KCNE1
1 µA
2 s
+KCNE1
2 µA
2 s
G/GMax
1
0.75
0.5
0.25
0
-120 -60 0 60 120
V (mV)
E
KCNQ1F0R/H5E
−KCNE1
1 µA
2 s
+KCNE1
2 µA
2 s
G/GMax
1
0.75
0.5
0.25
0
-120 -60 0 60 120
V (mV)
F
KCNQ1F0R
-20 +40 -40
% Inh
100
80
60
40
20
0
XE991
Chromanol
2 s
0.5 µA
G
KCNQ1F0R/D202N
% Inh
100
80
60
40
20
0
XE991
Chromanol
2 s
0.5 µA
H
KCNQ1F0R/Q3E
-20 +40 -40
% Inh
100
80
60
40
20
0
XE991
Chromanol
2 s
0.5 µA
I
KCNQ1F0R/R4E
% Inh
100
80
60
40
20
0
XE991
Chromanol
2 s
0.5 µA
J
KCNQ1F0R/H5E
% Inh
100
80
60
40
20
0
XE991
Chromanol
2 s
0.5 µA